

Extreme Cardiac MRI Analysis under Respiratory Motion: Results of the CMRxMotion Challenge

Kang Wang^{a,b,1}, Chen Qin^{c,1}, Zhang Shi^{d,1}, Haoran Wang^{a,b}, Xiwen Zhang^{a,b}, Chen Chen^{e,f}, Cheng Ouyang^{e,g}, Chengliang Dai^e, Yuanhan Mo^g, Chenchen Dai^d, Xutong Kuang^h, Ruizhe Liⁱ, Xin Chenⁱ, Xiuzheng Yue^j, Song Tian^j, Alejandro Mora-Rubio^{k,l}, Kumaradevan Punithakumar^k, Shizhan Gong^m, Qi Dou^m, Sina Amirrajabⁿ, Yasmina Al Khalil^o, Cian M. Scannell^o, Lexiaozi Fan^p, Huili Yang^q, Xiaowu Sun^r, Rob van der Geest^r, Tewodros Weldebirhan Arega^s, Fabrice Meriaudeau^t, Caner Özer^u, Amin Ranem^v, John Kalkhof^v, İlkyay Öksüz^u, Anirban Mukhopadhyay^v, Abdul Qayyum^w, Moona Mazher^x, Steven A Niederer^w, Carles Garcia-Cabrera^y, Eric Arazo^z, Michal K. Grzeszczyk^{aa}, Szymon Płotka^{ab}, Wanqin Ma^{ac}, Xiaomeng Li^{ac}, Rongjun Ge^{ad}, Yongqing Kou^{ae}, Xinrong Chen^{a,b,af,ag}, He Wang^{ah}, Chengyan Wang^{d,*}, Wenjia Bai^{e,ai,aj,*}, Shuo Wang^{a,b,*}

^aDigital Medical Research Center, School of Basic Medical Sciences, Fudan University, Shanghai, Shanghai 200032, China

^bShanghai Key Laboratory of MICCAI, Fudan University, Shanghai, Shanghai 200032, China

^cDepartment of Electrical and Electronic Engineering & I-X, Imperial College London, London, London SW7 2AZ, United Kingdom

^dDepartment of Radiology, Zhongshan Hospital Affiliated to Fudan University, Shanghai, Shanghai 200032, China

^eDepartment of Computing, Imperial College London, London, London SW7 2AZ, United Kingdom

^fSchool of Computer Science, University of Sheffield, Sheffield, S1 4DP, United Kingdom

^gDepartment of Engineering Science, University of Oxford, Oxford, OX2 0ES, United Kingdom

^hShanghai Pudong Hospital and Human Phenome Institute, Fudan University, Shanghai, 201203, China

ⁱSchool of Computer Science, University of Nottingham, Nottingham, NG8 1BB, United Kingdom

^jClinical & Technical Support, Philips Healthcare, Beijing, Beijing 100600, China

^kRadiology and Diagnostic Imaging, University of Alberta, Edmonton, AB T6G 1K4, Canada

^lDepartamento de Electrónica y Automatización, Universidad Autónoma de Manizales, Manizales 170001, Caldas, Colombia

^mDepartment of Computer Science and Engineering, The Chinese University of Hong Kong, Hong Kong, Hong Kong 000000, China

ⁿThe D-Lab, Department of Precision Medicine, GROW - Research Institute for Oncology and Reproduction, Maastricht University, 6220 MD Maastricht, The Netherlands

^oDepartment of Biomedical Engineering, Eindhoven University of Technology, Eindhoven 5612 AZ, The Netherlands

^pDepartment of Radiology, Northwestern University, 737 N. Michigan Ave, Suite 1600, Chicago 60611, United States

^qUnited Imaging Research, 393 Middle Huaxia Road, Pudong, Shanghai 201210, China

^rDivision of Image Processing, Department of Radiology, Leiden University Medical Center, PO Box 9600, Leiden 2300 RC, The Netherlands

^sUniversité Bourgogne Europe, ImVia UR 7535, 21000 Dijon, France

^tUniversité Bourgogne Europe, CNRS, ICMUB UMR 6302, 21000 Dijon, France

^uIstanbul Technical University, Maslak, 34467, İstanbul, Türkiye

^vComputer Science, Technical University of Darmstadt, Karolinenpl. 5, 64289 Darmstadt, Germany

^wNational Heart and Lung Institute, Faculty of Medicine, Imperial College London, Guy Scadding Building, Cale Street, London, SW3 6LY, United Kingdom

^xHawkes Institute, Department of Computer Science, University College London, 66-72 Gower St, London, United Kingdom

^ySchool of Medicine, University College Dublin, Belfield, Dublin, D04 VIW8, Ireland

^zCeADAR: Ireland's Centre for AI, University College Dublin, Belfield, Dublin, D04 VIW8, Ireland

^{aa}Sano Centre for Computational Medicine, Czarnowiejska 36, 30-054, Krakow, Poland

^{ab}Faculty of Mathematics and Computer Science, Jagiellonian University, S. Łojasiewicza 6, Krakow, Poland

^{ac}Department of Electronic and Computer Engineering, The Hong Kong University of Science and Technology, Clear Water Bay, Hong Kong 000, China

^{ad}School of Instrument Science and Engineering, Southeast University, Nanjing, Nanjing 210096, China

^{ae}College of Artificial Intelligence, Nanjing University of Aeronautics and Astronautics, Nanjing, Nanjing 211106, China

^{af}Academy for Engineering and Technology, Fudan University, Shanghai, Shanghai 200433, China

^{ag}College of Biomedical Engineering, Fudan University, Shanghai, Shanghai 200433, China

^{ah}Institute of Science and Technology for Brain-inspired Intelligence, Fudan University, Shanghai, Shanghai 200433, China

^{ai}Department of Brain Sciences, Imperial College London, London, London SW7 2AZ, United Kingdom

^{aj}Data Science Institute, Imperial College London, London, London SW7 2AZ, United Kingdom

Abstract

Deep learning models have achieved state-of-the-art performance in automated Cardiac Magnetic Resonance (CMR) analysis. However, the efficacy of these models is highly dependent on the availability of high-quality, artifact-free images. In clinical practice, CMR acquisitions are frequently degraded by respiratory motion, yet the robustness of deep learning models against such artifacts remains an underexplored problem. To promote research in this domain, we organized the *MICCAI CMRxMotion* challenge. We curated and publicly released a dataset of 320 CMR cine series from 40 healthy volunteers who performed specific breathing protocols to induce a controlled spectrum of motion artifacts. The challenge comprised two tasks: 1) automated image quality assessment to classify images based on motion severity, and 2) robust myocardial segmentation in the presence of motion artifacts. A total of 22 algorithms were submitted and evaluated on the two designated tasks. This paper presents a comprehensive overview of the challenge design and dataset, reports the evaluation results for the top-performing

*Corresponding authors: Shuo Wang (shuowang@fudan.edu.cn), Chengyan Wang (wangcy@fudan.edu.cn), Wenjia Bai (w.bai@imperial.ac.uk).

¹These authors contributed equally.

methods, and further investigates the impact of motion artifacts on five clinically relevant biomarkers. All resources and code are publicly available at: <https://github.com/CMRxMotion>.

Keywords: Cardiac magnetic resonance, image quality assessment, image segmentation, respiratory motion artifacts, model robustness

1. Introduction

Cardiac magnetic resonance (CMR) imaging is the gold-standard modality for evaluating cardiac structure and function (Schulz-Menger et al., 2020). In terms of image analysis, deep learning approaches have achieved remarkable performance in automated CMR image segmentation (Chen et al., 2020; Bai et al., 2020). However, the generalizability of these segmentation models is still challenged by inconsistent imaging environments (e.g., different vendors or protocols) (Campello et al., 2021), population shifts (normal vs. pathological cases) (Bernard et al., 2018) and unexpected human behaviors (e.g., body movements). To build a reliable segmentation model, it is useful to investigate when and how the model fails (Wang et al., 2020) by exposing a trained segmentation model to extreme cases in a stress test (Eche et al., 2021), such as altered image quality caused by motion artifacts that may occur during clinical practice. To date, most CMR image segmentation challenges have focused on vendor variability (Campello et al., 2021), and anatomical structure variations (Bernard et al., 2018; Martín-Isla et al., 2023), while the implications of human behaviors are less explored. For CMR image analysis, respiration motion is one of the major human behaviors that influence image quality (Ferreira et al., 2013). Patients may not be able to follow breath-hold instructions well, particularly those with heart failure or pediatric patients. Poor breath-hold behaviors result in degraded image quality and inaccurate analysis of cardiac structures (Wang et al., 2021b). To establish a public benchmark dataset for assessing the effects of respiratory motion on CMR quality and examining the robustness of segmentation models (Paschali et al., 2018), we organized the extreme CMR image analysis challenge under respiratory motion challenge (*CMRxMotion*) at *MICCAI 2022*².

To curate an extreme CMR dataset with respiratory motion artifacts, one way is to screen retrospective images stored in the hospital imaging database and identify those problematic ones. This requires considerable human efforts for screening and it is often restricted by data governance regulations. It may also introduce confounding factors such as vendors, scan protocols, and pathologies that are difficult to disentangle from respiratory motion. Instead, we design a prospective study in which healthy volunteers are recruited to perform different breath-hold behaviors during one imaging visit using the same scanner. As the confounding factors of MRI equipment and scan protocols are controlled, the curated CMR dataset is established in specific to respiratory motion artifacts. This manuscript is structured following the Biomedical Image Analysis Challenges (BIAS) guideline (Maier-Hein et al., 2020), and it provides a comprehensive summary of the *CMRxMotion Challenge*, including the data acquisition protocol, data annotation procedures,

evaluation tasks and metrics, ranking methodology, award scheme, and challenge results.

2. Related work

Over the past two decades, a multitude of challenges focused on cardiac chamber segmentation have been instrumental in advancing the field. These events provide a standardized platform for the objective comparison of algorithms, fostering innovation in clinical and research applications. This section reviews the evolution of these challenges to contextualize the unique contribution of *CMRxMotion*, which, as summarized in Table 1, is the first to specifically address the robustness of segmentation models to respiratory motion artifacts.

Early challenges primarily targeted the segmentation of core cardiac structures in both healthy and pathological cases, namely the left ventricle (LV), right ventricle (RV), and left ventricular myocardium (MYO). For instance, given the clinical importance of the LV ejection fraction (EF) as a predictor of heart disease (Bristow et al., 2017), foundational challenges such as the Sunnybrook Cardiac Data (SCD) (Radau et al., 2009) and the LV Segmentation Challenge (LVSC) (Suinesiaputra et al., 2014) centered on the LV and MYO. Similarly, to address the need for automated evaluation of the RV in conditions like dysplasia and cardiomyopathy (Mast et al., 2017), the Right Ventricle Segmentation Challenge (RVSC) was established to benchmark methods for delineating the RV endocardium and epicardium (Petitjean et al., 2015).

As the field matured, the scope of these challenges expanded significantly. The focus shifted towards more complex and clinically relevant problems, including multi-structure segmentation, cross-domain generalization, and the analysis of pathological tissue. Challenges began to incorporate a wider range of anatomical targets, such as the atria (Tobon-Gomez et al., 2015; Xiong et al., 2021) and, in some cases, the entire heart (Zhuang et al., 2019). Concurrently, a major focus became assessing model robustness to data heterogeneity. This was addressed by curating datasets from multiple institutions, featuring different scanner vendors, imaging protocols, and diverse patient populations (Zhuang, 2019; Campello et al., 2021; Martín-Isla et al., 2023). More recently, challenges have also begun to target the direct segmentation of pathological tissue, such as myocardial scar and edema in the MyoPS challenge (Li et al., 2023).

Despite this progress in tackling data heterogeneity, the challenge landscape has largely overlooked the critical problem of image quality degradation from patient motion, a factor that frequently compromises the clinical utility of automated methods. In clinical practice, poor breath-holding is a

²<http://cmr.miccai.cloud>

Table 1: Precedent related challenges for cardiac MR image segmentation. CMR: Cardiac Magnetic Resonance, SSFP: steady-state free precession sequences, bSSFP: balanced steady-state free precession sequences, LGE: Late gadolinium enhancement, MI: myocardial infarction, MH: myocardial hypertrophy, NHP: normal healthy subject, DCM: dilated cardiomyopathy, HCM: Hypertrophic Cardiomyopathy, CAM: Congenital Arrhythmogenesis, ARR: Arrhythmogenic cardiomyopathy, HF: Heart Failure, TF: Tetralogy of Fallot, AF: Atrial Fibrillation, IC: Interatrial Communication, TR: Tricuspidal Regurgitation, ARV: abnormal right ventricle, LA: Left atrium, RA: Right atrium, LV: left ventricle, MYO: left ventricular myocardial, RV: right ventricle, PV: Pulmonary vein, AO: Ascending aorta, SAX: short axis, LAX: long axis, N/A: Not reported, \dagger : The data reported only provided the number of MR images, without additional details.

Challenge	Challenge Name	Year	Reference	Data Information and Data Split					Segmentation Target	Pathologies	Scanner	Held in Conjunction
				Sequence	Data \dagger	Training \dagger	Testing \dagger					
SCD	Sunnybrook Cardiac Data (Cardiac MR Left Ventricle Segmentation Challenge data)	2009	Radau et al. (2009)	SSFP	45	45	-		LV, MYO	HF, HCM, NHS	GE Signa 1.5T	MICCAI 2009
LVSC	LV Segmentation Challenge	2011	Sunesiaputra et al. (2014)	SAX and LAX SSFP	200	100	100		LV, MYO	MI	GE Signa 1.5T, Philips Achieva (1.5T, 3.0T, and Intera 1.5T), and Siemens (Avanto 1.5T, Espree 1.5T and Symphony 1.5T)	MICCAI 2011
RVSC	Right Ventricle Segmentation Challenge	2012	Petitjean et al. (2015)	bSSFP	48	16	32		RV	N/A	Siemens Symphony Tim 1.5T	MICCAI 2012
LASC'13:	Left Atrial Segmentation Challenge	2013	Tobon-Gomez et al. (2015)	bSSFP	30	10	20		LA, PV	N/A	Philips Achieva 1.5T	MICCAI 2013
MM-WHS	Multi-Modality Whole Heart Segmentation	2017	Zhuang et al. (2019)	bSSFP	60	20	40		LV, RV, LA, RA, MYO, AO	DCM	Philips 1.5T, Siemens Magnetom Avanto 1.5T	MICCAI 2017
ACDC	Automated Cardiac Diagnosis Challenge	2017	Bernard et al. (2018)	1.5T and 3T, SSFP	150	100	50		LV, RV, MYO	NOR, MI, HCM, ARV	Siemens Area and Trio Tim	MICCAI 2017
ASC	Atria Segmentation Challenge	2018	Xiong et al. (2021)	LGE	154	100	54		LA	AF	GE-MRIs	MICCAI 2018
MSCMR	Multi-sequence Cardiac MR Segmentation Challenge	2019	Zhuang (2019)	LGE, T2 and bSSFP	115	75	40		LV, RV, MYO	MI, DCM	Philips Achieva 1.5 T	MICCAI 2019
M&Ms-1	Multi-Centre, Multi-Vendor & Multi-Disease Cardiac Image Segmentation Challenge	2020	Campello et al. (2021)	N/A	375	175	200		LV, RV, MYO	MH, DCM, NHS	Siemens MAGNETOM (Avanto and Skyra) Philips Achieva GE Signa Excite Canon Vantage Orian	MICCAI 2020
MyoPS 20	Myocardial pathology segmentation combining multi-sequence CMR	2020	Li et al. (2023)	bSSFP, T2 CMR	45	25	20		MYO Scar, MYO Edema	MI	Philips Achieva 1.5T	MICCAI 2020
M&Ms-2	Multi-Disease, Multi-View & Multi-Center Right Ventricular Segmentation in Cardiac MRI	2020	Martín-Isla et al. (2023)	N/A	360	200	160		LV, RV, MYO	DCM, HCM, CAM, ARR, TF, IC, TR, NHS	Siemens, General Electric, and Philips	MICCAI 2021

common occurrence, leading to artifacts that degrade image quality, blur anatomical boundaries, and introduce heterogeneous intensity distributions (Wang et al., 2021b). Such artifacts can severely compromise the performance of segmentation models trained exclusively on high-quality data, leading to inaccurate analysis and potentially erroneous clinical conclusions. To date, no challenge has provided a framework to *stress test* algorithms against this common source of failure. Therefore, evaluating model performance in the presence of motion artifacts is essential for developing truly robust and clinically trustworthy tools (Paschali et al., 2018).

To address this critical gap, we organized the *CMRxMotion* challenge. Its primary goal was to establish the first benchmark for a twofold problem: first, the automated assessment of CMR image quality itself, and second, the evaluation of segmentation model robustness in the presence of motion artifacts. By providing a curated dataset with controlled motion degradation, this challenge aims to drive the development of reliable analysis tools that are resilient to the image quality issues frequently encountered in real-world clinical practice.

3. Materials and methods

3.1. Data acquisition

The study received ethical approval from the institutional review board of Fudan University (FE20017), and all participants provided written informed consent. The cohort consisted of 40 healthy volunteers (24 male, 16 female) with an age range of 19 to 48 years and a bodyweight range of 45 to 85 kg. All imaging was performed on a 3T MRI scanner (Siemens MAGNETOM Vida) at the Zhangjiang International Brain Imaging Center, Fudan University. We employed a clinical TrueFISP balanced Steady-State Free Pre-

cession (bSSFP) cine sequence, following the protocols detailed in our previous work (Wang et al., 2021a). For this challenge, we released short-axis (SAX) image volumes at the end-diastolic (ED) and end-systolic (ES) frames. The acquisition parameters were set to an in-plane spatial resolution of 2.0×2.0 mm, a slice thickness of 8.0 mm, and a slice gap of 4.0 mm.

To generate a dataset with a controlled spectrum of image quality, we intentionally deviated from the standard operating procedure (SOP) for breath-holding. Each volunteer underwent four separate scans during a single imaging session, each with a different breathing instruction: a) adhere to the breath-hold requirements; b) halve the breath-hold period; c) breathe freely; and d) breathe intensively. This protocol yielded a grouped set of CMR images for each volunteer, capturing a range of motion artifact severity from none (high-quality) to severe. From each of the four acquisitions, 3D image volumes at the ED and ES frames were extracted, resulting in a total of eight volumes per volunteer and 320 volumes for the entire dataset. Fig. 1 demonstrates an example of the resulting motion-degraded images.

3.2. Preprocessing

All acquired short-axis cine images were processed through a standardized pipeline. First, the DICOM files were anonymized and subsequently converted to the NIfTI format using the *dicom2nifti* Python package³. From each 4D cine sequence, the 3D image volumes corresponding to the end-diastolic (ED) and end-systolic (ES) frames were extracted. Finally, to ensure compatibility with various NIfTI viewers such as ITK-SNAP, orientation information was removed from the image headers. This process yielded a total of 320 3D image volumes for the challenge dataset.

³<https://dicom2nifti.readthedocs.io/en/latest/>

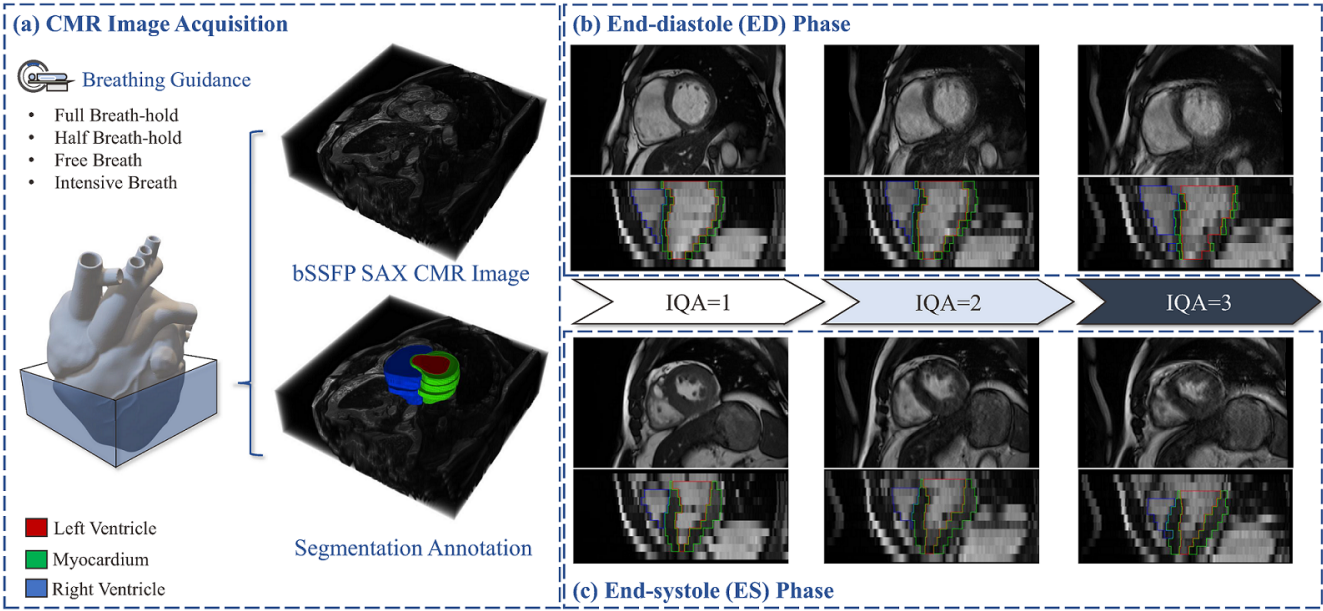


Figure 1: Visualization example of paired short-axis (SAX) CMR images with different Image Quality Assessment (IQA) scores, acquired from the same volunteer performing four distinct breath-hold behaviors following specific breathing guidance during CMR acquisition. (b) End-diastolic (ED) images, showing three images with progressively increasing IQA scores, are presented in the top row. (c) End-systolic (ES) images, which also display three CMR scans in both axial and coronal planes, are presented in the bottom row.

3.3. Challenge dataset

The 320 image volumes were partitioned at the subject level to prevent data leakage between sets. The dataset was randomly split as follows: a **training set** of 160 volumes (20 volunteers), a **validation set** of 40 volumes (5 volunteers), and a **test set** of 120 volumes (15 volunteers). The training data, along with corresponding ground truth annotations, were released to all registered participants. The validation images were also released, but their annotations were withheld to power a live leaderboard for online evaluation. Both the images and annotations for the test set were fully withheld and used exclusively for the final, offline evaluation of submitted containerized algorithms. All annotations were manually delineated by radiologists with over six years of experience. Following the conclusion of the challenge, the data and annotations remain publicly accessible under a CC-BY non-commercial license to encourage further research.

4. Challenge design

The *CMRxMotion challenge* was organized by a collaborative team of researchers from Fudan University, the University of Edinburgh, Imperial College London, the University of Oxford, and Zhongshan Hospital. The challenge was designed to establish a benchmark for two critical, unsolved problems in automated CMR analysis: the image quality assessment (IQA) and the robust cardiac segmentation (RCS) in the presence of respiratory motion.

4.1. Task 1: automated image quality assessment

4.1.1. Motivation

CMR images that are severely degraded by motion artifacts are often diagnostically unacceptable and may necessitate re-acquisition, leading to increased scan time and patient discomfort. The development of an automated IQA model capable of identifying such low-quality images could provide immediate, real-time feedback to MR technologists, improving clinical workflow efficiency. The primary objective of Task 1 was, therefore, to benchmark algorithms for the automated evaluation of respiratory motion artifacts in CMR images.

4.1.2. Annotation protocol

The image quality of all 320 volumes was manually assessed by two experienced radiologists (Z.S. and C.D.) using 3D Slicer⁴. Following a consensus meeting to establish a standardized protocol. The standard 5-point Likert scale is defined as follows: excellent diagnostic quality (5), more than adequate for diagnosis (4), adequate for diagnosis (3), questionable for diagnosis (2), and non-diagnostic (1). For better reproducibility, three levels of motion artifacts are defined based on the original 5-point scores. For the purpose of creating a well-defined classification task, these five scores were consolidated into three final labels, as detailed in Table 3. Images with scores of 4 or 5 were categorized as having **mild motion** (Label 1), images with a score of 3 were categorized as having **intermediate motion** (Label 2), and images with scores of 1 or 2 were categorized as having **severe motion** (Label 3). The objective for participants was to develop a model that predicts one of these three labels for a given input image volume.

⁴<http://www.slicer.org>

Table 3: Assessment criteria for subjective image quality and label definition in Task 1.

5-point Likert Scale	Subjective Image Quality Grade	Details	IQA Label
V	Excellent	No artifacts present	
IV	More than adequate for diagnosis	Minor artifacts present but image quality somewhat reduced	1
III	Adequate for diagnosis	Minor artifacts present and image quality somewhat reduced but still sufficient for diagnosis	2
II	Questionable for diagnosis	Image quality impaired by artifacts so diagnostic value of images is questionable	3
I	Non-diagnostic	Image quality heavily impaired by artifacts and readers not able to assess	

4.1.3. Evaluation metrics

Cohen’s Kappa statistics is used to evaluate the model performance in this task. It is a common metric to measure the level of agreement between two raters who classify items into mutually exclusive categories (Benchoufi et al., 2020):

$$\kappa = \frac{p_o - p_e}{1 - p_e} \quad (1)$$

where p_o is the observed agreement ratio (overall accuracy of the model) and p_e is the agreement between the prediction and the ground truth as if happening by chance. Participating teams submitted a containerized Docker image designed to predict a label from the set $\{1, 2, 3\}$, corresponding to mild, intermediate, and severe motion artifacts. We calculate the weighted Cohen’s Kappa between the submission and the manual annotation.

For a more detailed performance analysis, we also computed several secondary metrics: Accuracy, Precision, and Recall. Accuracy measures the overall proportion of correctly classified samples:

$$\text{Accuracy} = \frac{1}{N} \sum_{i=1}^N \mathbf{1}\{\hat{y}_i = y_i\} \quad (2)$$

where N is the total number of samples, and \hat{y}_i and y_i are the predicted and true labels. $\mathbf{1}\{\cdot\}$ represents the indicator function, which equals 1 if the condition is true, and 0 otherwise.

Precision and Recall were calculated on a per-class basis. Precision for class k is the ratio of true positive predictions to the total number of instances predicted as class k :

$$\text{Precision}_k = \frac{TP_k}{TP_k + FP_k} \quad (3)$$

where TP_k is the number of true positives and FP_k is the number of false positives for class k . Recall for class k is the proportion of true positives among all samples that truly belong to class k :

$$\text{Recall}_k = \frac{TP_k}{TP_k + FN_k} \quad (4)$$

where FN_k is the number of false negatives for class k . It is important to note that these secondary metrics were used for descriptive analysis only and did not contribute to the final ranking. All metrics were calculated using the *scikit-learn* Python package⁵.

4.1.4. Ranking scheme

The final ranking on the test set was generated by sorting the submissions based on their Cohen’s Kappa scores. To evaluate whether the performance differences between algorithms were statistically significant, we performed bootstrap sampling to calculate the 95% confidence intervals (95% CI) for each submission’s score.

4.2. Task 2: robust cardiac segmentation

4.2.1. Motivation

Learning-based segmentation models are known to be susceptible to failure when encountering images with quality characteristics unseen during training. The objective of Task 2 was to challenge participants to develop segmentation models that are robust to the presence of respiratory motion artifacts.

4.2.2. Annotation protocol

The segmentation annotation protocol followed the standards of previous CMR challenges. Manual contours were delineated for the LV and RV blood pools and the MYO. Critically, segmentation masks were only generated for images deemed to be of diagnostic quality (i.e., those with an IQA score of 1 or 2 from Task 1). The annotations were performed by an experienced technician (X.K.) using 3D Slicer and subsequently reviewed and refined by two senior radiologists (Z.S. and C.D.). The final segmentation masks used the following label definitions: 0 (Background), 1 (LV), 2 (MYO), and 3 (RV). Fig. 2 provides a visualization of the segmentation labels.

4.2.3. Evaluation metrics

Segmentation performance was evaluated using two standard metrics: the Dice Similarity Coefficient (DSC) and the 95th percentile of the Hausdorff Distance (HD95). The DSC measures the volumetric overlap between the ground truth (X) and the predicted segmentation (Y):

$$\text{DSC} = \frac{2|X \cap Y|}{|X| + |Y|} \quad (5)$$

The HD95 measures the 95th percentile of the maximum surface distance between the contours of the two masks, providing a robust measure of boundary accuracy:

$$\text{HD95} = \max_{x \in X} \{P_{95\%} d(x, Y), P_{95\%} d(y, X)\} \quad (6)$$

⁵<https://scikit-learn.org/>

where $d(x, Y) = \min_{y \in Y} \|x - y\|$. Both metrics were calculated using the MedPy library⁶.

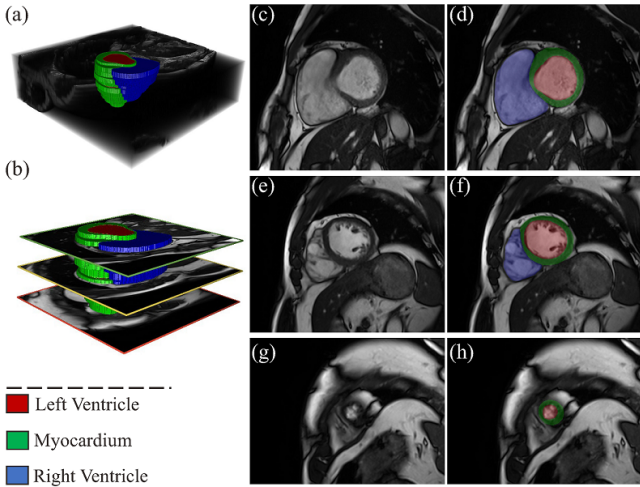


Figure 2: Visualization of segmentation labels for Task 2. (a) Volume rendering of a short-axis CMR image. (b) Volume rendering of the corresponding segmentation mask. (c-h) Paired image slices and segmentation masks for the basal, mid-ventricular, and apical regions. The LV is shown in red, MYO in green, and RV in blue.

4.2.4. Ranking scheme

To determine the final ranking, we employed a *rank-then-aggregate* strategy. For each case in the test set, we first ranked all participating teams based on their DSC and HD95 scores for each of the three structures (LV, MYO, and RV). This process resulted in six individual rankings per case for each team. The final ranking score for each team was then calculated as the average of all these individual ranks across all test cases. This method ensures that the final ranking reflects consistent performance across all structures and metrics, rather than being skewed by exceptional performance on a single metric. The Wilcoxon signed-rank test was used to assess the statistical significance of differences between the final ranking scores of the teams.

4.3. Rules and timeline schedule

4.3.1. Rules

The challenge was governed by a set of rules designed to ensure a fair, transparent, and reproducible evaluation.

- 1. Submission policy:** The challenge consisted of two main phases. During the validation phase, participants were permitted to make up to three submissions per day to a live leaderboard for each task. For the final testing phase, each team was allowed a single submission of a containerized Docker image for the official offline evaluation. Besides, members of the organizers could not participate in the challenge.
- 2. Use of external data:** Teams were permitted to use publicly available external data for model training. However, all external data sources were required to

be explicitly cited and described in the accompanying methodology paper. This rule was intended to encourage the exploration of techniques such as transfer learning and domain adaptation.

- 3. Reproducibility:** To ensure the replicability of results, participants were required to submit a manuscript detailing their methods. For the final testing phase, a self-contained Docker image, including all source code and pretrained model weights, was mandatory. Public release of the code was strongly encouraged to benefit the wider research community.
- 4. Automation and fairness:** All submitted algorithms had to be fully automatic, with no manual intervention permitted during inference. To ensure a standardized and fair evaluation environment, network access was strictly prohibited during the execution of the Docker containers on the test set.

4.3.2. Timeline

The *CMRxMotion* challenge was a one-time event, with foundational work (including data collection, processing, annotation, and visual inspection) conducted between May 2021 and April 2022. During this period, the challenge proposal was formulated and submitted, receiving official acceptance from the *MICCAI 2022* Satellite Events Committee on February 28, 2022. The public phase of the competition began with the launch of the official website on April 1, 2022, with participant registration opening shortly after on April 15. The training dataset—complete with images and ground truth labels—along with a brief challenge description paper (Wang et al., 2022), was released to all registered teams on May 31. The validation phase commenced on July 1 with the release of the validation images and the opening of the live leaderboard on the Synapse platform⁷. In parallel, the test set was annotated by three senior radiologists. The final testing phase was initiated on September 1 with the launch of the Docker submission platform for offline evaluation. The challenge culminated at the *MICCAI 2022* conference. Top-performing teams were invited to submit full papers, which, after peer review, were published in the *STACOM* workshop proceedings. The top three winning teams for each task presented their work at the workshop held on September 18, 2022, where they were officially recognized and awarded.

4.3.3. Infrastructure

The challenge was supported by a comprehensive technical infrastructure distributed across several platforms, each serving a specific function:

- 1. Challenge homepage:** The official website (<http://cmr.miccai.cloud>) served as the central information hub for participant registration, rules, timelines, and data usage agreements.
- 2. Validation platform:** The Synapse platform (<https://www.synapse.org/#!Synapse:syn32407769/wiki/>) was used for secure data distribution and to

⁶<http://loli.github.io/medpy/>

⁷<https://www.synapse.org/#!Synapse:syn32407769/wiki/>

host a live leaderboard for real-time, automated evaluation of submissions.

3. **Testing platform:** A dedicated platform (<https://docker.miccai.cloud>) managed the collection and execution of containerized Docker submissions on a standardized GPU environment for the final, offline evaluation.
4. **Public archives:** To ensure long-term accessibility, all resources are publicly archived. A GitHub repository (<https://github.com/CMRxMotion>) provides access to evaluation scripts and code, while the submitted Docker images are archived on Docker Hub (<https://hub.docker.com/repositories/cmrxmlmotion>) under an Apache 2.0 license.

5. Submission and evaluation

The evaluation procedure for the *CMRxMotion challenge* was conducted in two distinct stages: a validation phase with a live leaderboard, and a final testing phase based on containerized algorithm submissions. This two-stage design allowed for iterative development while ensuring a final, definitive ranking on unseen data.

5.1. Validation phase

During the validation phase, participants could benchmark their models using the provided training set (160 volumes from 20 volunteers) and submit predictions for the validation set (40 volumes from 5 volunteers). To facilitate iterative refinement, teams were permitted up to three submissions per day to a live leaderboard for each task.

For the **IQA task**, submissions were in the form of a comma-separated values (CSV) file containing the predicted quality label {1, 2, 3} for each validation case. An automated backend calculated the Cohen’s Kappa score against the withheld ground truth and updated the leaderboard. For the **RCS task**, participants submitted a compressed archive of their predicted segmentation masks in NIfTI format. The backend computed the Dice Similarity Coefficient (DSC) and 95% Hausdorff Distance (HD95) for the LV, MYO, and RV. It is important to note that images with severe motion artifacts (IQA Label 3) were excluded from the segmentation evaluation due to the lack of reliable ground truth annotations.

5.2. Testing phase

The final ranking was determined through an offline evaluation on a sequestered test set (120 volumes from 15 volunteers). For this phase, each team submitted a self-contained Docker image of their algorithm, including all source code and pretrained model weights. This approach ensured reproducibility and prevented overfitting to the validation set leaderboard. All submissions were executed in a standardized, isolated environment on a GPU server with the following specifications: 10 CPU cores (2.50 GHz), 32 GB RAM, and an NVIDIA Tesla V100 GPU (32 GB VRAM). To ensure fairness, network access was disabled, and a maximum inference time of four hours was allotted for each task.

The final ranking for the **IQA task** was determined by sorting submissions in descending order of their Cohen’s

Kappa score on the test set. For the **RCS task**, the final ranking was based on a robust *rank-then-aggregate* strategy. For each test case, we ranked all teams based on their DSC and HD95 scores for each of the three structures (LV, MYO, and RV). The final score for each team was the average of these individual ranks across all cases. This method, which aligns with conventions established in previous segmentation challenges (e.g., (Maier et al., 2017; Baid et al., 2021)), rewards consistently high performance across all metrics and anatomical structures. The Wilcoxon signed-rank test was subsequently employed to assess whether the differences in final ranking scores between teams were statistically significant—that is, whether the higher-ranked methods demonstrated a statistically significant advantage over the lower-ranked ones.

6. Results

The *CMRxMotion challenge* garnered substantial interest from the research community, with formally 112 registered participants and a total of 275 and 340 submissions to the validation leaderboard for Task 1 and Task 2, respectively. For the final testing phase, 10 teams submitted Docker images for the IQA task, and 13 teams submitted for the RCS task. The top-3 teams were invited to present their work at the *STACOM* satellite workshop at *MICCAI 2022*, and 14 methodology papers were accepted into the workshop proceedings (Camara et al., 2023). This section presents the performance of the submitted algorithms, providing an overview of all participating methods included in this benchmark. Publicly available resources (e.g., publications, released code, and Docker images) are summarized in Table 4.

6.1. Performance analysis of the IQA task

Ten teams successfully completed the final testing phase for the IQA task. An overview of their methodologies is presented in Table 5. The primary ranking metric for the IQA task was the linearly weighted Cohen’s Kappa (κ), chosen for its robustness in multiclass classification scenarios with potential class imbalance. The final results are reported in Table 6, with overall accuracy provided as a supplementary, non-ranking metric.

The submitted algorithms demonstrated a wide range of performance on the test set, with Kappa scores ranging from -0.075 to 0.631. The winning team, A1.UON_IMA, achieved a Kappa score of 0.631 and an accuracy of 0.725. The second and third-place teams, A2.Philips_CTS and A3.OpenGTN, also delivered strong results, with Kappa scores of 0.549 and 0.474, respectively. A common strategy among the top three teams was the use of pre-training on external datasets, which appeared to confer a significant performance advantage. To assess the statistical significance and stability of these rankings, we performed a bootstrap analysis with 10,000 samples. The resulting 95% confidence intervals (CI) for the Kappa scores are visualized in Fig. 5. The winning team’s score had a tight 95% CI of [0.518, 0.734], indicating a consistently superior performance. The CIs for the subsequent ranks were wider, with considerable overlap among the teams ranked 4th through 8th, suggesting their performance was statistically similar.

Table 4: Overview of all workshop papers accepted in the STACOM proceedings, along with the publicly available or otherwise accessible reproducible resources provided by the corresponding participating teams. TID denotes the team identifier for Task 1 (TID prefixed with A) and Task 2 (TID prefixed with S). Checkmark (✓) indicates that the team participated in the corresponding task or has made the relevant resources available.

TID	Team	References	Participating		Source Code		Docker Image		Publicly Accessible and Reproducible Resources
			Task1	Task2	Task1	Task2	Task1	Task2	
A1	UON_IMA	Li and Chen (2022)	✓		✓		✓		<ul style="list-style-type: none"> • Source Code: https://github.com/ruienze-1/CMRxMotion • Docker Image: https://hub.docker.com/r/cmrxmlotion/a1.uon_ima
S2	Med-Air	Gong et al. (2022)		✓		✓		✓	<ul style="list-style-type: none"> • Source Code: https://github.com/CMRxMotion/S2.Med-Air • Docker Image: https://hub.docker.com/r/cmrxmlotion/s2.med-air
A2/S7	Philips.CTS	Li et al. (2022)	✓	✓	✓	✓	✓	✓	<ul style="list-style-type: none"> • Source Code: https://github.com/CMRxMotion/A2_S7.Philips_CTS • Docker Image 1: https://hub.docker.com/r/cmrxmlotion/a2.philips_cts • Docker Image 2: https://hub.docker.com/r/cmrxmlotion/s7.philips_cts
A3/S5	OpenGTN	Amirrajab et al. (2022)	✓	✓	✓	✓	✓	✓	<ul style="list-style-type: none"> • Source Code: https://github.com/CMRxMotion/A3_S5.OpenGTN • Docker Image 1: https://hub.docker.com/r/cmrxmlotion/a3.opengtn • Docker Image 2: https://hub.docker.com/r/cmrxmlotion/s5.opengtn
A4	issun	Sun et al. (2022)	✓		✓		✓		<ul style="list-style-type: none"> • Source Code: https://github.com/CMRxMotion/A4.issun • Docker Image: https://hub.docker.com/r/cmrxmlotion/a4.issun
A5/S4	Tewodros	Arega et al. (2022)	✓	✓	✓	✓	✓	✓	<ul style="list-style-type: none"> • Source Code: https://github.com/tewodrosweledebirhan/cardiac_segmentation_cmrxmlotion2022 • Docker Image: https://hub.docker.com/r/cmrxmlotion/s4.tewodros
A6/S3	CMR.Love.LHND	Yang et al. (2022)	✓	✓	✓	✓	✓	✓	<ul style="list-style-type: none"> • Source Code: https://github.com/CMRxMotion/A6_S3.CMR.Love.LHND • Docker Image 1: https://hub.docker.com/r/cmrxmlotion/a6.cmr.love.lhnd • Docker Image 2: https://hub.docker.com/r/cmrxmlotion/s3.cmr.love.lhnd
A7/S8	MI-IST_DA	Ranem et al. (2022b)	✓	✓	✓	✓	✓	✓	<ul style="list-style-type: none"> • Source Code: https://github.com/MECLabTUDA/QA_med_data/tree/CMRxMotion • Docker Image 1: https://hub.docker.com/r/cmrxmlotion/a7.mi-ist_da • Docker Image 2: https://hub.docker.com/r/cmrxmlotion/s8.mi-ist_da
A8/S1	UA-SVCC	Mora-Rubio et al. (2022)	✓	✓	✓	✓	✓	✓	<ul style="list-style-type: none"> • Source Code: https://github.com/CMRxMotion/A8_S1.UA-SVCC • Docker Image 1: https://hub.docker.com/r/cmrxmlotion/a8.ua-svcc • Docker Image 2: https://hub.docker.com/r/cmrxmlotion/s1.ua-svcc
A9/S6	Abdul	Qayyum et al. (2022)	✓	✓	✓	✓	✓	✓	<ul style="list-style-type: none"> • Source Code: https://github.com/RespectKnowledge/CMRxMotion_Solution • Docker Image 1: https://hub.docker.com/r/cmrxmlotion/a9.abdul • Docker Image 2: https://hub.docker.com/r/cmrxmlotion/s6.abdul
S9	ML-Labs	Garcia-Cabrera et al. (2022)	✓		✓		✓		<ul style="list-style-type: none"> • Source Code: https://github.com/CMRxMotion/S9.ML-Labs • Docker Image: https://hub.docker.com/r/cmrxmlotion/s9.ml-labs
A10/S10	Sano	Grzeszczyk et al. (2022)	✓	✓	✓	✓	✓	✓	<ul style="list-style-type: none"> • Source Code: https://github.com/CMRxMotion/A10_S10.Sano • Docker Image 1: https://hub.docker.com/r/cmrxmlotion/a10.sano • Docker Image 2: https://hub.docker.com/r/cmrxmlotion/s10.sano
S11	HAHA2	Ma et al. (2022)	✓		✓		✓		<ul style="list-style-type: none"> • Source Code: https://github.com/MAWanqin2002/STACOM2022Ma • Docker Image: https://hub.docker.com/r/cmrxmlotion/s11.haha2
S12	sots	Kou et al. (2022)		✓		✓		✓	<ul style="list-style-type: none"> • Source Code: https://github.com/CMRxMotion/S12.sots • Docker Image: https://hub.docker.com/r/cmrxmlotion/s12.sots

A detailed breakdown of per-class performance is provided by the confusion matrixes in Fig. 3 and the precision-recall analysis in Fig. 4. These results highlight a key challenge: while most algorithms performed well in identifying images with mild motion (Label 1), their performance degraded significantly for images with intermediate (Label 2) and, particularly, severe motion (Label 3). As shown in Fig. 4 (b), the recall for severe motion artifacts was generally low across all teams, indicating that these cases were the most difficult to correctly classify. This suggests that while current methods are effective at identifying high-quality images, accurately classifying the degree of severe motion artifacts remains a significant area for future improvement.

6.2. Overview of IQA methodologies

The ten submitted solutions for the IQA task were all based on machine learning, with a strong predominance of deep learning techniques. A summary of the methods and their configurations is provided in Table. 5.

6.2.1. Architectures and training paradigms

All submitted algorithms predominantly employed deep learning (DL) methods, involving convolutional neural networks (CNNs) or Transformer architectures. Notably, one team (Li et al., 2022) integrated DL techniques with classical machine learning models (including Extra Trees, Random Forest, Decision Tree, and GDBOost classifiers) by leveraging radiomics-derived features. The adopted end-to-end learning frameworks incorporated many state-of-the-art (SOTA) classification models. Popular choices of CNN backbones included the ResNet (He et al., 2016) and EfficientNet (Tan and Le, 2019) families. Transformer-based models included Vision Transformers (ViT) and Swin Transformers. As shown in Table. 6, it worth to note a notable

trend that lightweight backbones (Li et al., 2022; Arega et al., 2022; Yang et al., 2022) often achieved competitive or even superior performance, possibly due to a reduced risk of overfitting on the limited dataset. The majority of participating teams adopted 2D models that processed CMR volumes in a slice-wise manner, which generally outperformed their 3D counterparts.

Most teams utilized a standard, end-to-end supervised training framework. However, several explored alternative paradigms to boost performance. Multi-task learning was adopted by some, either by treating IQA as the primary task with an auxiliary objective (Arega et al., 2022) or vice versa (Grzeszczyk et al., 2022). Pre-training emerged as a particularly effective strategy, with several top teams leveraging transfer learning from models pre-trained on ImageNet (Li and Chen, 2022). Self-supervised pre-training (SSP) was also successfully employed, using techniques like SimSiam (Chen and He, 2021) to enhance representation learning (Li et al., 2022) or by training an autoencoder to reconstruct clean images from synthetically corrupted ones with simulated motion artifacts (Amirrajab et al., 2022).

6.2.2. Ensemble strategies

Model ensembling was a key strategy for many of the top-performing teams. These approaches varied in complexity and design, encompassing architectural ensembles and data-level ensembles (e.g., combining models at the slice level and volume level). The winning team, UON_IMA, developed a hierarchical ensemble that first combining predictions from different 2D CNN and ViT models at the slice level, and then aggregating these into a final volume-level prediction using a custom voting scheme (Li and Chen, 2022). Another successful approach, proposed by Philips_CTS through the RE-Vote framework, combined a

Table 5: Overview of top 10 methods for IQA task. Type represents the method employ 2D or 3D method. w/o denotes the presence of a given setting, w/o denotes its absence, and n/a indicates that the corresponding result was not reported in the original paper. Ensemble represents the ensemble models during inference time. TTA denotes test time augmentation. ViT represents vision transformer and Swin represents Swin-transformer. SSP represents reconstruction self-supervised pretraining. CNN represents Self-constructed CNN.

Team	Type	Deep Learning Model		Machine Learning Model	Image Preprocessing	Data Augmentation	External Data	Pretraining	Ensemble		TTA Models
		CNN Backbone	Transformer Backbone						Method	Method	
A1. UON_IMA	2D	ResNet EfficientNet	ViT	w/o	Calculating 2D gradient magnitude map	n/a	w/o	ImageNet pre-training	Majority voting	Majority voting	6 w/o
A2. Philips_CTS	3D	EfficientNet(FF-b0)	w/o	Extra trees, random forest, decision tree, and GDBoost.	Cropping or padding to 512x512	Random scale and crop, horizontal flipping, and intensity shift	w/o	Simsiam on training set	Majority voting	Majority voting	5 w/o
A3. OpenGTN	2D	Autoencoder	w/o	w/o	K-space motion artifact simulation	n/a	M&Ms1	SSP on training set and M&Ms1	n/a	n/a	w/o
A4. issun	2D	ResNet	w/o	w/o	Scale normalization, min-max intensity normalization	Weighted image interpolation from same subject, histogram matching with interpolation	w/o	n/a	w/o	w/o	w/
A5. Tedodros	3D	ResNet-18	w/o	w/o	Resampling, z-score intensity normalization	Random scaling and cropping, random rotation, random flipping	w/o	n/a	Mean average	Mean average	2 w/
A6. CMR.love.LHND	2D	CNN	w/o	w/o	Image padding	Vertical flip, horizontal flip, and image rotation	w/o	w/o	w/o	w/o	w/
A7. MI-IST_DA	2D	ResNet-152 EfficientNet(FF-b5)	w/o	w/o	Min-max intensity normalization, Center crop	Random affine transformations	w/o	n/a	CORN, CORAL	CORN, CORAL	5 w/o
A8. UA-SVCC	2D	EfficientNet(FF-b7)	w/o	w/o	Decompose the MR images into 2D slices	Random 90° rotations, flips, zooms, random Gaussian sharpen and smoothing operations to simulate motion artifacts	w/o	n/a	w/o	w/o	w/o
A9. Abdul	3D	DenseNet-201	w/o	w/o	Cropping, resampling, z-score intensity normalization	Vertical Flip, Horizontal Flip, Random Gamma, zoom, random rotate	w/o	w/o	w/o	w/o	w/o
A10. Sano	3D	w/o	Swin Transformer	w/o	z-score intensity normalization	Random flips, random zoom, random rotate	w/o	n/a	5-Fold Ensemble	5-Fold Ensemble	5 w/o

Note: Deep learning (DL) models refer to architectures based on convolutional neural networks (CNNs), Transformers, and multilayer perceptrons (MLPs), whereas machine learning models refer to classical machine learning approaches such as random forests. SimSiam represents a self-supervised pretraining framework, while CORN and CORAL are learning-based model ensemble methods. 5-Fold in the ensemble column denotes ensembleing models obtained from 5-fold cross-validation.

Table 6: Results of the IQA task. Acc represents accuracy and the data representation mode is mean [95% CI lower, 95% CI upper]. 95% CI represents 95% confidence interval. TID represents the team identifier. Values highlighted in bold red denote the best performance, whereas those in bold black indicate the second-best results.

Rank	TID	Team	Acc [95% CI]	Cohen's Kappa [95% CI]
1	A1	UON_IMA	0.725 [0.642, 0.800]	0.631 [0.518, 0.734]
2	A2	Philips_CTS	0.708 [0.625, 0.792]	0.549 [0.419, 0.670]
3	A3	OpenGTN	0.625 [0.542, 0.708]	0.474 [0.357, 0.582]
4	A4	issun	0.642 [0.558, 0.725]	0.456 [0.328, 0.580]
5	A5	Tewodros	0.608 [0.525, 0.692]	0.455 [0.341, 0.564]
6	A6	CMR.love.LHND	0.650 [0.567, 0.733]	0.447 [0.333, 0.561]
7	A7	MI-IST_DA	0.633 [0.550, 0.717]	0.433 [0.325, 0.542]
8	A8	UA-SVCC	0.608 [0.517, 0.692]	0.432 [0.317, 0.540]
9	A9	Abdul	0.567 [0.483, 0.650]	0.382 [0.258, 0.499]
10	A10	Sano	0.400 [0.317, 0.483]	-0.075 [-0.203, 0.053]

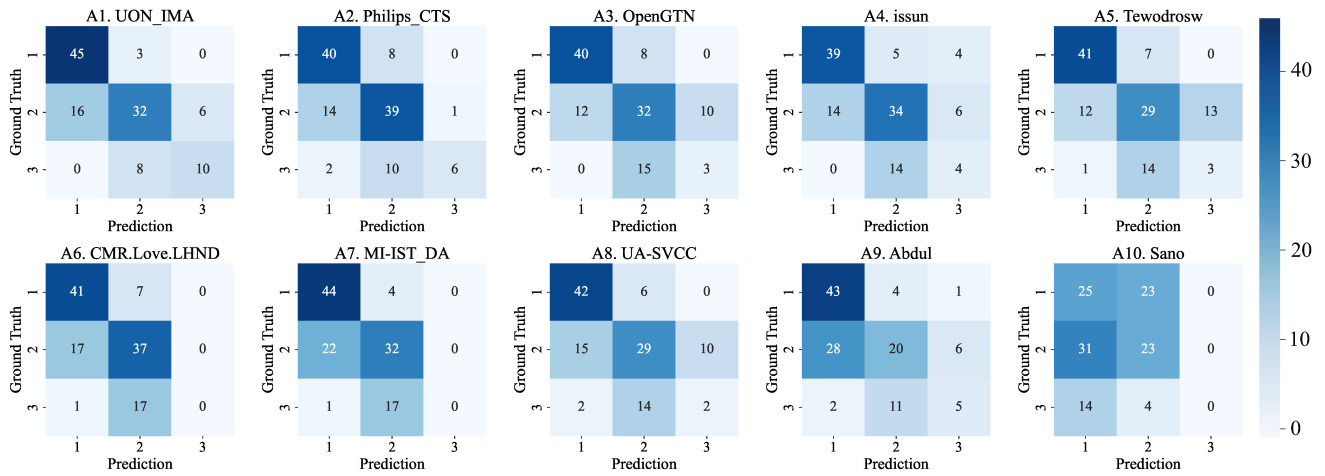


Figure 3: Confusion matrixes for the IQA task. The horizontal axis represents the predicted labels, and the vertical axis represents the ground truth labels.

deep learning model with four classical machine learning classifiers trained on radiomic features (Li et al., 2022). Learning-based ensembles, such as rank-consistent networks like CORAL (Cao et al., 2020) and CORN (Shi et al., 2023) also exhibited performance advantages over individual models. Simpler but still effective ensemble methods included combining models trained with different loss functions (Arega et al., 2022) or aggregating predictions from models trained across different cross-validation folds (Mora-Rubio et al., 2022).

6.2.3. Data preprocessing and augmentation

Nearly all teams employed a series of preprocessing steps to standardize the input data. Common techniques included resampling to a uniform voxel spacing, as well as cropping and padding to a fixed volume size. For intensity normalization, both z-score standardization and min-max scaling were widely used. Some teams also incorporated more specialized preprocessing, such as generating 2D gradient maps as an additional input modality (Li and Chen, 2022) or simulating motion artifacts in k-space (Amirrjab et al., 2022).

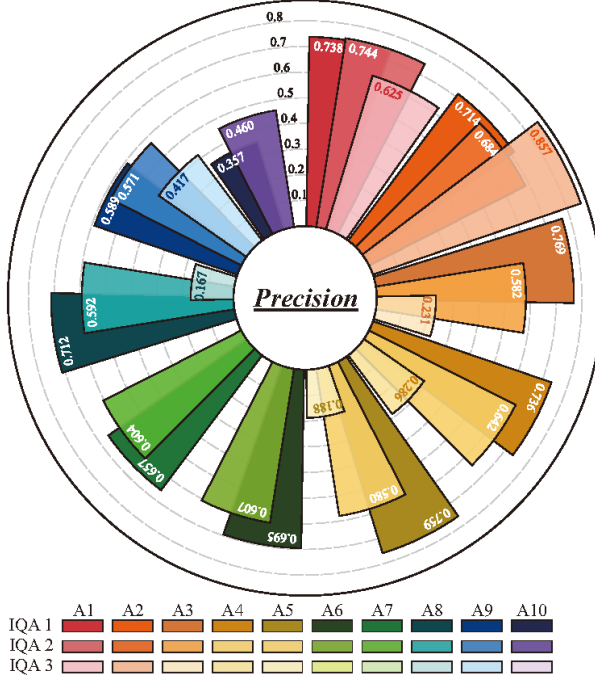
Data augmentation was universally applied to increase the diversity of the training set and improve model robustness. Standard spatial augmentations included random rotations, scaling, cropping, and flips. Intensity-based augmentations involved adjustments to brightness and contrast, as

well as the application of Gaussian blurring and sharpening to simulate motion-like effects. Several teams also employed Test-Time Augmentation (TTA), where multiple augmented versions of a test image are evaluated and their predictions averaged to produce a more robust final output (Sun et al., 2022; Arega et al., 2022; Yang et al., 2022).

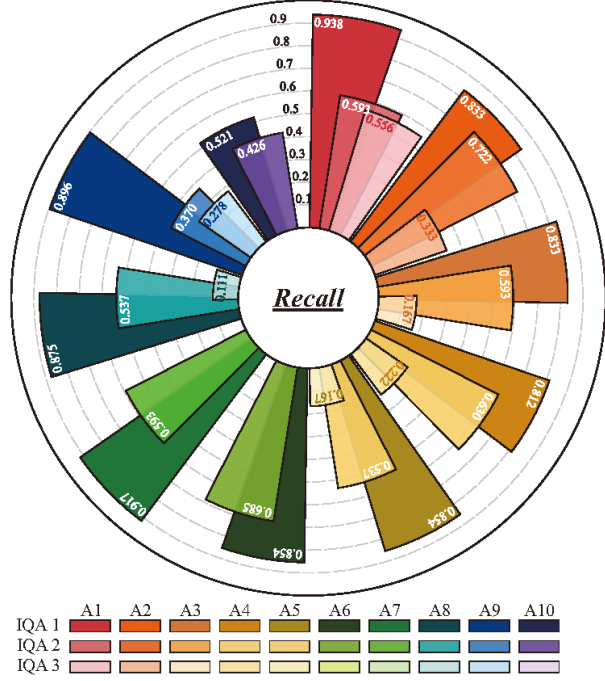
6.3. Details of IQA algorithms

6.3.1. A1. UON_IMA

The team UON_IMA (Li and Chen, 2022) won first place in the IQA task. They developed an ensemble learning framework incorporating several 2D advanced classification models (i.e., ResNet (He et al., 2016), EfficientNet (Tan and Le, 2019), and ViT (Dosovitskiy et al., 2020)) pretrained on ImageNet (Deng et al., 2009) on both the original intensity images and the 2D in-plane gradient magnitude maps. Observations indicated that slices from the apical and basal regions may contribute minimally to the overall IQA score. To address this, the method first employs a U-Net (Ronneberger et al., 2015) to locate and sample image patches around the foreground region. Six classification models are then applied, derived by training each of the three base architectures (ResNet, EfficientNet, ViT) separately on both image modalities (intensity and gradient). The final predictions are integrated using a hierarchical voting strategy: after obtaining scores for each slice, a subject-level decision is made for each model using a bias voting scheme on the



(a) Analysis of Precision Metrics in IQA Task



(b) Analysis of Recall Metrics in IQA Task

Figure 4: Nightingale rose chart illustrating the per-class classification performance for the IQA task in terms of (a) Precision and (b) Recall. Each colored group corresponds to a participating team, and the three sectors within each group represent performance on the three IQA labels.

slice-level predictions. These subject-level predictions are then combined via a final majority vote. The bias voting scheme incorporates weighting factors derived from 5-fold cross-validation on the training set. The proposed ensemble method demonstrates robustness and efficiency on both the validation and testing datasets, outperforming other approaches as presented in Table. 6 and Fig. 5.

6.3.2. A2. Philips_CTS

The team Philips_CTS (Li et al., 2022) also employed an ensemble framework using both DL models and machine learning approaches based on radiomics, achieving second place in the IQA task. The deep-learning model employed is a lightweight EfficientNet-B0 (Tan and Le, 2019). To mitigate overfitting due to the limited dataset size, self-supervised pretraining—specifically SimSiam (Chen and He, 2021)—was utilized to enhance representation learning and alleviate overfitting in EfficientNet-B0. Subsequently, the authors applied four machine learning models (Extra Trees, Random Forest, Decision Tree, and Gradient Boosting (GDBoost) classifiers) to generate radiomics-based predictions based on 50 selected features, which were extracted and selected via PyCaret (Ali, 2020) from the LV regions identified and cropped using nnU-Net (Isensee et al., 2021). By employing a weighted voting mechanism — assigning weights of 0.2 to deep learning and 0.8 to the radiomics models—Philips_CTS achieved a Cohen’s Kappa score of 0.549, with a 95% CI of [0.419, 0.670].

6.3.3. A3. OpenGTN

The OpenGTN (Amirrajab et al., 2022) team secured third place by training an autoencoder—a 2D U-Net-like model without skip connections—to take input images

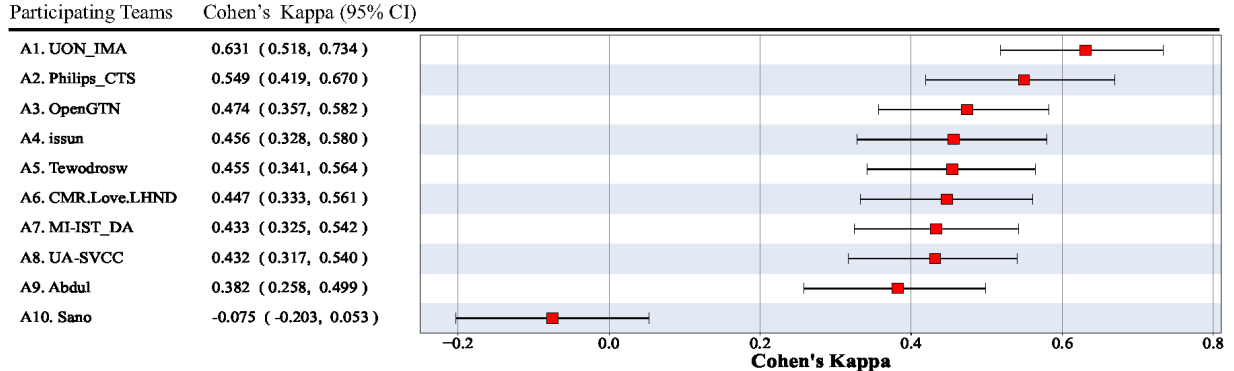
with simulated motion artifacts and reconstruct the original artifact-free images. Following this motion-denoising self-supervised pretraining, the encoder was connected to two fully connected layers to predict the IQA score for each slice. The final IQA score for the entire image volume was obtained by averaging the slice-level scores and applying a conditional decision rule. To augment the training dataset, k-space motion artifact simulation was used to generate SSP training data. This was achieved by introducing simulated artifacts into motion-free images from the *CMRxMotion* training dataset, as well as incorporating additional data from the M&Ms-1 challenge (Campello et al., 2021). With this approach and the implementation of targeted data augmentation strategies, OpenGTN achieved a Cohen’s Kappa score of 0.474, with a 95% CI of [0.357, 0.582].

6.3.4. A4. issun

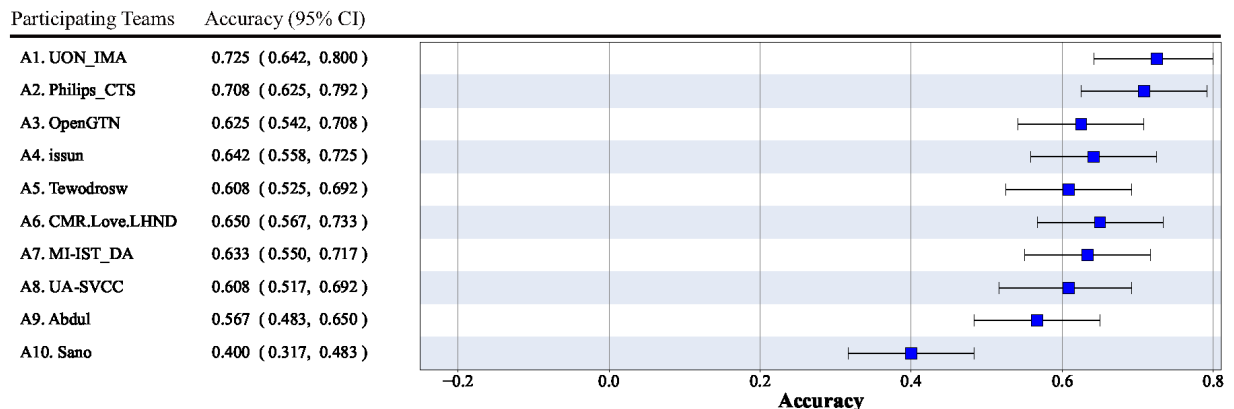
Team issun (Sun et al., 2022) introduced a two-branch sampling inspection network with dedicated data augmentation techniques for IQA task. The network emulates human visual inspection by applying two distinct random slice sampling strategies—one per branch. Each branch employs ResNet as its backbone to extract features, which are then fused through a dedicated fusion module to generate the final IQA score.

6.3.5. A5. Tewodros

Team Tewodros (Arega et al., 2022) developed a multi-task learning framework based on 3D ResNet-18 (He et al., 2016), incorporating a second classification branch to predict the patient’s breath-hold type as an auxiliary task. This multi-task setup demonstrated significant improvements over single-task IQA prediction. To further enhance



(a). Forest plot of Cohen's Kappa performance



(b). Forest plot of Accuracy performance

Figure 5: Forest plots of IQA performance. The means (depicted as red and blue squares) and the 95% confidence intervals (shown as horizontal lines) are estimated from 10,000 bootstrap samples of the image quality assessment task on the test dataset. The x-axis represents the metric values, while the y-axis denotes the participating teams. The horizontal lines indicate the 95% confidence intervals (95% CI) derived from the bootstrap analysis. The means (represented by red and blue squares) are calculated by averaging the respective metric across all cases of test set.

prediction accuracy, the method applies TTA techniques, averaging predictions over M augmented samples to produce the final output. Additionally, an ensemble of models—comprising both single-task and multi-task variants trained with different loss functions (focal loss and weighted cross-entropy)—provided an additional performance gain. With this comprehensive strategy, Team Tewodros secured 5th place in the benchmark.

6.3.6. A6. CMR.Love.LHND

Subsequently ranked in the benchmark is Team CMR.Love.LHND (Yang et al., 2022), which treated the IQA task as a quality control problem and developed a lightweight 2D CNN model. By incorporating basic techniques such as residual connections, the team achieved a balance between strong performance and memory efficiency, with the model requiring only 3 GB of video memory. To further enhance performance, TTA techniques were employed, averaging predictions across three image transformations to produce more robust motion-level estimations. Notably, while this method achieved the highest score on the live validation leaderboard, it ultimately placed sixth on the final test set.

6.3.7. A7. MI-IST_DA

Team Aranme (Ranem et al., 2022b) introduced the rank-consistent neural network, namely CORAL (Cao et al.,

2020) and CORN (Shi et al., 2023), to make the final decisions using several binary classifiers while taking into account the rank consistency among predictions. By using CORAL and adopting EfficientNet-B5 as the backbone, a significant improvement over ResNet-152 is observed in the IQA task. This method secured the 6th place in our benchmark.

6.3.8. A8. UA-SVCC

Team UA-SVCC (Mora-Rubio et al., 2022) employed EfficientNet-b7 (Tan and Le, 2019) for the IQA task. To train this large-scale backbone, the team used a weighted loss function along with the Nadam optimizer (Dozat, 2015). The CMR volumes were decomposed into 2D slices, and a variety of augmentation techniques were applied, including random 90° rotations, flips, and zooms. Additionally, random Gaussian sharpening and smoothing operations were introduced to simulate the effects of respiratory motion artifacts.

6.3.9. A9. Abdul

Team Abdul (Qayyum et al., 2022) introduced a 3D DenseNet-201 architecture comprising four dense blocks, each containing six layers, based on the work of (Huang et al., 2017). This design leverages dense connectivity to address the vanishing gradient problem, enhance feature propagation, encourage feature reuse, and reduce the overall

number of parameters. In the proposed framework, only a small subset of features is added at each layer, while the remaining feature maps are preserved and reused throughout the network. The final decision layer utilizes all accumulated feature maps, enabling comprehensive representation learning. This approach not only reduces parameter count but also improves the flow of information and gradients, simplifying the training process. Importantly, each layer has direct access to the loss gradients and input data, enforcing an implicit deep supervision mechanism that facilitates training of deeper networks. Additionally, the dense connections exhibit a regularizing effect, which helps mitigate overfitting even with limited training data.

6.3.10. A10. Sano

Team Sano (Grzeszczyk et al., 2022) adopted a multi-task learning framework for simultaneous IQA and segmentation, based on the Swin-UNETR architecture (Hatamizadeh et al., 2022). In this design, a 3D Swin Transformer encoder, originally used for segmentation, is connected to additional fully connected layers following global average pooling and dropout. This auxiliary branch is responsible for predicting the IQA score in parallel with the segmentation task. The final IQA score is obtained by ensembling predictions from models trained using a 5-fold cross-validation strategy. However, this approach did not yield a significant improvement in kappa score, potentially due to the substantial task differences between segmentation and IQA, or as a result of overfitting on the validation or local dataset.

6.4. Performance analysis of the RCS task

Thirteen teams successfully completed the final testing phase for the RCS task. This section provides a detailed analysis of the submitted algorithms' performance, followed by an overview of the common methodological themes that emerged from the top-performing solutions. An overview of the specific methods is provided in Table. 7.

The quantitative results for all participating teams are summarized in Table. 8. The submitted algorithms achieved a wide range of segmentation accuracies. The average Dice Similarity Coefficient (DSC) scores across all teams ranged from 81.81% to 93.90% for the LV, 67.73% to 87.37% for the MYO, and 63.95% to 92.22% for the RV. The corresponding average 95% Hausdorff Distance (HD95) values ranged from 3.05 mm to 15.21 mm for the LV, 2.20 mm to 17.53 mm for the MYO, and 3.53 mm to 21.16 mm for the RV.

Consistent with previous cardiac segmentation challenges, the MYO proved to be the most challenging structure to segment, primarily due to its thin anatomical structure. In contrast, the LV and RV blood pools were generally segmented with higher accuracy. In terms of the DSC metric, the top performance for LV segmentation was achieved by UA-SVCC (93.90%), while Med-Air obtained the best scores for the MYO (87.38%) and RV (92.39%). For the HD95 metric, Tewodros obtained the lowest HD95 distance for the LV (2.95 mm) and MYO (2.11 mm), while UA-SVCC obtained the best performance for the RV (3.53 mm).

The final ranking was determined using a robust rank-then-aggregate strategy, with the Wilcoxon signed-rank test used to assess statistical significance. This analysis resulted in a tie for first place between S1.UA-SVCC and S2.Med-Air, and a tie for second place between S3.CMR.Love.LHND and S4.Tewodros. The box plots in Fig. 6 illustrate the distribution of scores, showing that while the top teams achieved similar median performances, the winning methods exhibited greater consistency with tighter distributions and fewer outliers. The qualitative results in Fig. 8 further highlight that segmentation of the basal and apical slices was particularly challenging across all methods.

6.5. Overview of RCS methodologies

The submitted solutions for the RCS task were dominated by deep learning-based approaches, with several common themes emerging in terms of network architecture, training strategies, and data handling.

6.5.1. Architectures and training paradigms

For RCS task, the vast majority of submissions were based on the encoder-decoder architecture like U-Net (Ronneberger et al., 2015) or the U-Net variants (Qayyum et al., 2022; Garcia-Cabrera et al., 2022), with the nnU-Net framework (Isensee et al., 2022) being particularly popular. Seven of the twelve teams employed nnU-Net either as their primary model, as a key component within an ensemble, or as a critical stage in a multi-step pipeline. Other architectures included Transformer-based models, such as Swin-UNETR (Hatamizadeh et al., 2022) and ViT U-Net (Ranem et al., 2022a). Although these generally did not outperform the top CNN-based approaches, particularly for the fine-structured MYO, they showed promising results in segmenting larger, convex-shaped structures such as the LV and RV. As shown in Fig. 7, most teams opted for 2D models, which is a common and effective strategy for CMR due to the anisotropic resolution of typical SAX acquisitions.

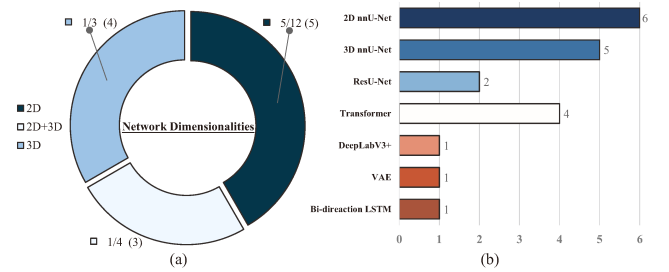


Figure 7: Overview of (a) model dimensionalities and (b) network architectures adopted by the participating teams in the RCS task.

In terms of training paradigms, most teams employed an end-to-end supervised framework, commonly using a combination of Dice and cross-entropy losses. Several teams explored more advanced strategies, such as multi-stage training with different loss functions (Mora-Rubio et al., 2022), two-stage coarse-to-fine segmentation (Li et al., 2022; Qayyum et al., 2022), and multi-task learning (Grzeszczyk et al., 2022; Kou et al., 2022). Pre-training on large external datasets (both natural images (Deng et al., 2009) and medical CMR images (Radau et al., 2009; Petitjean et al., 2015;

Table 7: Overview of RCS methods. Type represents the method employ 2D or 3D method. w/ denotes the presence of a given setting, w/o denotes its absence, and n/a indicates that the corresponding result was not reported in the original paper. Ensemble represents the ensemble models during inference time. TTA represent the cross entropy loss, and HD represent loss function based on Hausdorff Distance.

Team	Type	CNN Backbone	Transformer backbone	Preprocessing	Postprocessing	Data Augmentation	Pseudo Label	External Data	Pretrained Model	Uncertainty Estimation Methods		
										TTA	Ensemble	Multi-stage
S1. UASVCC	2D	nnU-Net	w/o	nnU-Net preprocessing	SPP	Random 90 rotations, flips, zooms, random Gaussian sharpen and smoothing	w/o	w/o	w/o	w/o	w/o	FSL
S2. 2D, 3D nnU-Net	2D, 3D	nnU-Net	w/o	nnU-Net preprocessing	SPP	Random rotation, scaling, Gaussian noise, Gaussian blur, brightness, contrast, simulation of low resolution, gamma correction and mirroring, adversarial augmentation (AdvChain)	w/o	SCD, LASB ¹³ , PT on ACDC, M&Ms-1, RVSC, DSB M&Ms-2, MyoPS, CMRSeg w/	5-Fold Cross-validation	w/o	w/o	FSL
S2. Med-Air	2D	w/o	Swin-UNETR	Center Cropping, Intensity normalization (min-max)	SPP	ACDC, M&Ms-1, MyoPS, MS-CMRSeg	SSL on SCD, LASB ¹³ , RVSC, DSB, ACDC and PT on ACDC, M&Ms-1, M&Ms-2, MyoPS, MS-CMRSeg	5-Fold Cross-validation	w/o	w/o	w/o	FSL
S3. 2D w/o	2D	w/o	Swin-UNet			SSL on ImageNet and PT on ACDC, M&Ms-1, M&Ms-2, MyoPS, MS-CMRSeg						
S4. 3D Bi-direction LSTM	2D, 3D	nnU-Net	w/o	w/o	nnU-Net postprocessing	enhanced Gaussian noise, Gaussian blur, brightness, contrast, and gamma correction	w/o	w/o	Ensemble of a 2D and a 3D version	w/o	w/o	FSL
S5. 3D nnU-Net	3D	nnU-Net	w/o	Image resampling	n/a	k-space augmentation, brightness, contrast, gamma, Gaussian noise, blur, Elastic deformation, random rotation, random scaling, random flipping, and low spatial resolution simulation.	ACDC	n/a	DicePolyCE	w/o	w/o	FSL
S6. 2D nnU-Net	2D	nnU-Net	w/o	nnU-Net preprocessing	n/a	Augmentation with simulated motion artifacts	M&Ms-1, M&Ms-2	n/a	FocalTVersity Dice+CE	w/o	w/o	FSL
S7. 3D 3D-ResUnet	3D	nnU-Net	w/o	Resampling (nearest neighbor interpolation), Intensity Normalization (z-score)	Volume resizing (bilinear interpolation)	Horizontal Flip, Vertical Flip, Random Gamma	w/o	n/a	Cross-validation	Two stage	FSL, SSL	Dice+BCE
S8. 2D VIT U-Net V2	2D	VIT U-Net V2	w/o	Spatial normalization, intensity normalization (min-max)	n/a	Rotation, flipping, scaling, deformation of the original images, adding noise, brightness modification	w/o	n/a	Two stage	FSL, SSL	Dice+CE	
S9. 2D U-Net (ResNet10)	2D, 3D	nnU-Net	w/o	nnU-Net preprocessing	nnU-Net postprocessing	Augmentation with simulated motion artifacts, flipping, rotation	w/o	w/o	Ensemble of VIT U-Net V2, and nnU-Net (2D and 3D)	w/o	w/o	FSL
S10. 2D U-Net (ResNet10)	2D	U-Net (ResNet10)	w/o	Image resampling, orientation	w/o	Random Motion, Random Ghosting, Random Bias Field, Random Gamma	w/o	n/a		w/o	w/o	FSL
S11. 3D DenseBiasNet-VAE	3D	DenseBiasNet-VAE	w/o	Volume resizing, volume padding	n/a	Fourier transformation	w/	w/o		w/	w/o	FSL
S12. 3D DenseBiasNet-VAE	3D	DenseBiasNet-VAE	w/o	Intensity normalization (z-score)	n/a	TTA	w/o	w/o		w/o	w/o	FSL
S13. 3D DenseBiasNet-VAE	3D	DenseBiasNet-VAE	w/o	Volume resizing, volume padding	n/a	Random flip, random zoom, random rotation	w/o	w/o	5-Fold Cross-validation	w/o	w/o	FSL
S14. 3D DenseBiasNet-VAE	3D	DenseBiasNet-VAE	w/o	Intensity normalization (z-score)	n/a	Fourier transformation	w/	w/o		w/	w/o	FSL
S15. 3D DenseBiasNet-VAE	3D	DenseBiasNet-VAE	w/o	Volume resizing, volume padding	n/a	TTA	w/o	w/o		w/o	w/o	FSL

DSB: Second Annual Data Science Bowl. LASC'13: Left Atrial Segmentation Challenge 2013. RVSC: Right Ventricle Segmentation Challenge (RVSC).

SCD: Sunnybrook Cardiac Data (SCD), also known as the 2009 Cardiac MR Left Ventricle Segmentation Challenge data.

PT: Pre-training. SSL: Self-Supervised Learning. SPP: Specified Post-processing.

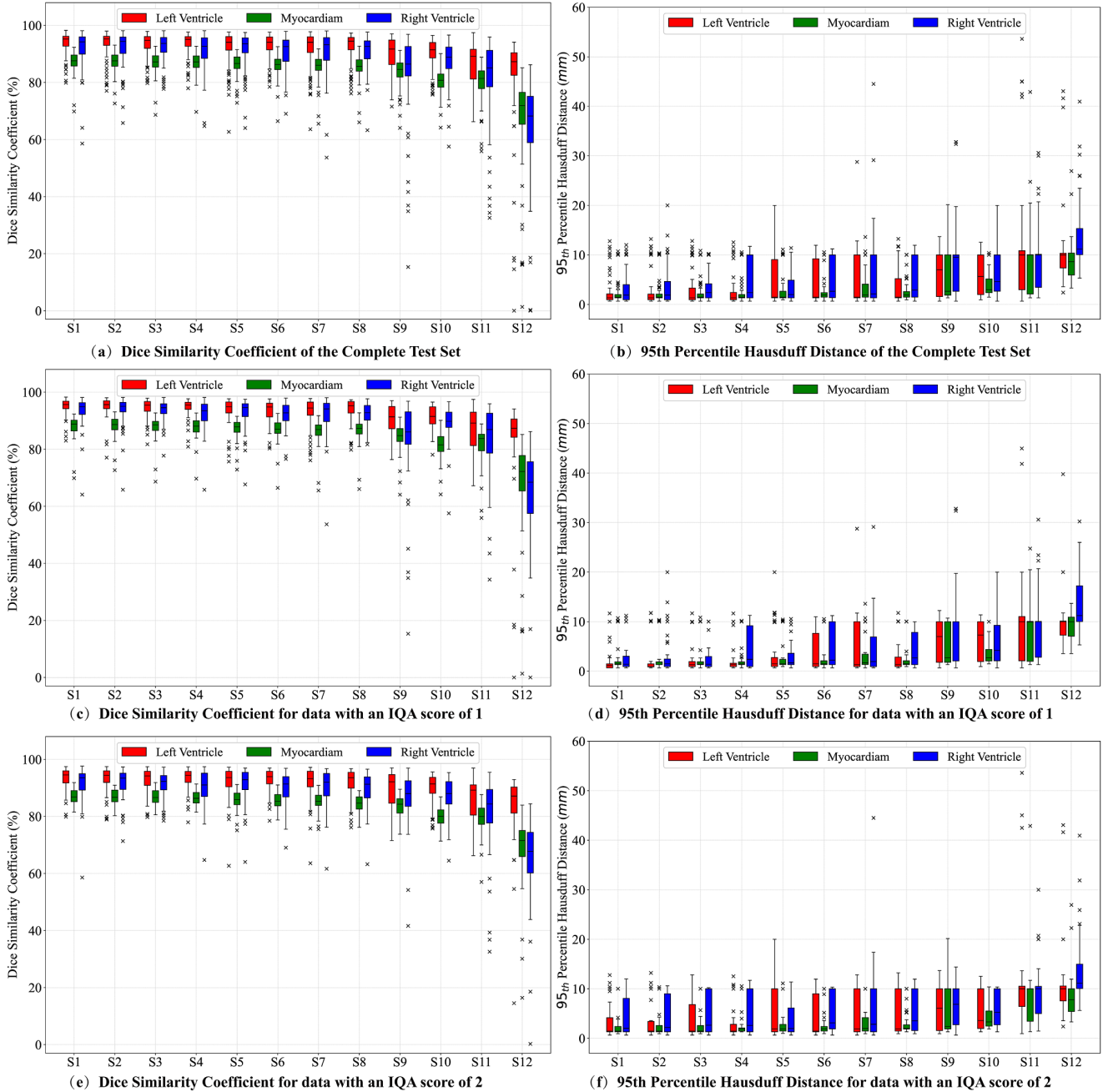


Figure 6: Box plots of the quantitative results for the robust segmentation task on the test set. The plots show the distribution of (a, c, e) Dice Similarity Coefficient and (b, d, f) 95th percentile Hausdorff Distance across the full test set and subsets with different IQA scores. The midline represents the median, and outliers are marked with \times .

Table 8: Performance of the RCS Task (Task 2). The reported data are presented in the format of mean \pm standard deviation. \uparrow indicates that higher values represent better performance, while a downward arrow (\downarrow) indicates that lower values are preferred. Values highlighted in bold red denote the best performance, whereas those in bold black indicate the second-best results. LV represents left ventricle, MYO represents myocardium, and RV represents right ventricle respectively.

Rank	Team	DSC (%) \uparrow			HD95 (mm) \downarrow		
		LV	MYO	RV	LV	MYO	RV
1	S1. UA-SVCC	93.90 \pm 3.72	87.37 \pm 3.36	92.22 \pm 6.07	3.05 \pm 3.54	2.20 \pm 2.10	3.53 \pm 3.55
	S2. Med-Air	93.72 \pm 4.32	87.38 \pm 3.25	92.39 \pm 5.52	3.13 \pm 3.71	2.57 \pm 2.70	3.59 \pm 3.85
2	S3. CMR.Love.LHND	93.41 \pm 4.10	87.06 \pm 3.56	92.34 \pm 4.40	3.42 \pm 3.74	2.37 \pm 2.26	3.68 \pm 3.40
3	S4. Tewodros	93.80 \pm 3.77	87.08 \pm 3.20	91.14 \pm 5.93	2.95 \pm 3.39	2.11 \pm 1.78	4.68 \pm 4.03
4	S5. OpenGTN	92.45 \pm 5.67	86.32 \pm 3.51	91.82 \pm 5.89	3.98 \pm 4.44	3.16 \pm 3.17	3.54 \pm 3.36
5	S6. Abdul	92.82 \pm 4.27	86.13 \pm 3.54	90.67 \pm 5.57	3.89 \pm 3.83	2.61 \pm 2.39	4.87 \pm 3.90
6	S7. Philips_CTS	91.90 \pm 6.15	85.54 \pm 4.09	90.75 \pm 7.15	4.92 \pm 7.47	3.66 \pm 3.41	5.13 \pm 6.20
7	S8. MI-IST_DA	92.53 \pm 5.04	85.55 \pm 3.93	90.80 \pm 5.40	3.76 \pm 3.85	2.76 \pm 2.48	4.87 \pm 3.71
8	S9. ML-Labs	89.65 \pm 6.29	83.69 \pm 4.55	84.22 \pm 13.68	6.17 \pm 4.22	5.03 \pm 4.06	7.69 \pm 5.98
9	S10. Sano	90.31 \pm 5.01	80.53 \pm 4.21	88.07 \pm 6.27	6.04 \pm 3.96	4.12 \pm 2.56	5.75 \pm 3.64
10	S11. HAHA2	86.59 \pm 7.52	80.25 \pm 6.18	81.51 \pm 14.00	12.26 \pm 14.91	7.63 \pm 5.69	9.28 \pm 6.42
	S12. sots	81.81 \pm 18.31	67.73 \pm 16.05	63.95 \pm 17.31	15.21 \pm 21.48	17.53 \pm 28.91	21.16 \pm 50.95

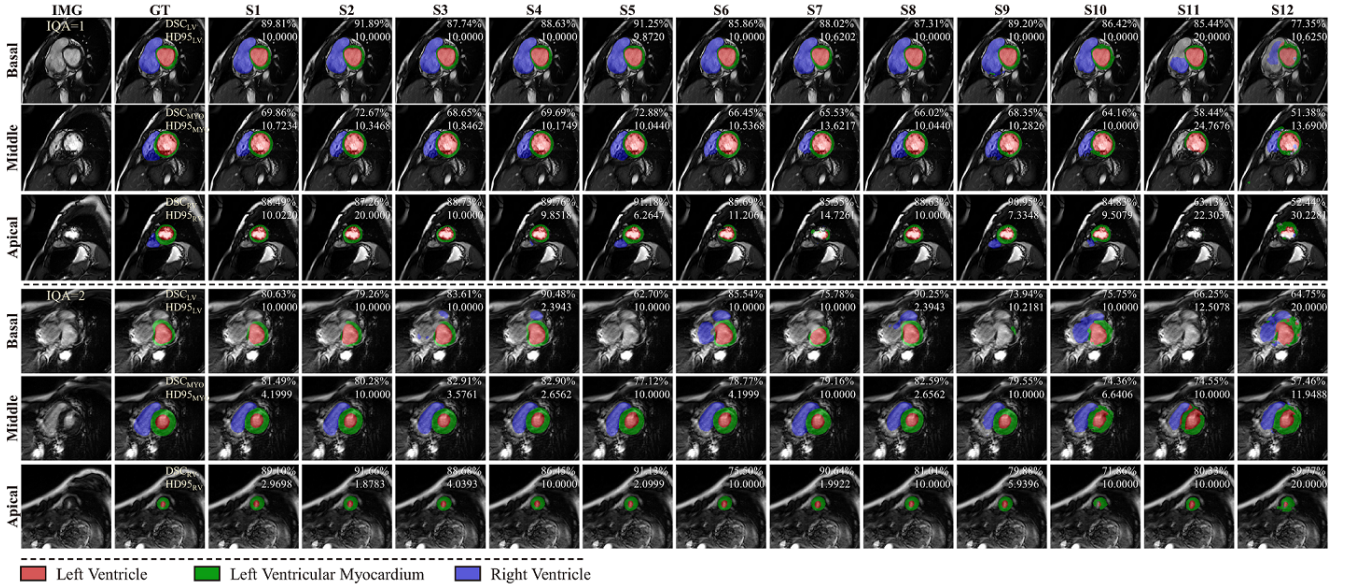


Figure 8: Qualitative segmentation results from all participants for two challenging cases with IQA scores of 1 (top three rows) and 2 (bottom three rows). For each case, the basal, middle, and apical slices are shown. GT denotes the ground truth.

Tobon-Gomez et al., 2015; A. et al., 2015)) and the use of semi-supervised techniques with pseudo-labeling were also feasible strategies to improve robustness.

6.5.2. Ensemble strategies

Model ensembling was a widely adopted and highly effective strategy. Common approaches included aggregating predictions from models trained across different cross-validation folds (Gong et al., 2022; Grzeszczyk et al., 2022; Qayyum et al., 2022) and combining different network dimensionalities (e.g., 2D and 3D models (Yang et al., 2022; Ranem et al., 2022b)), or architectures (e.g., CNNs and Transformers (Gong et al., 2022)) to leverage their complementary strengths. Some teams also developed more specialized ensemble frameworks, such as combining models trained with different data sampling strategies to better handle the challenging basal and apical slices (Amirrajab et al., 2022).

6.5.3. Data preprocessing and postprocessing

Nearly all participants utilized a comprehensive preprocessing pipeline. This typically involved spatial normalization (resampling to isotropic resolution, resizing, cropping, padding, and orientation normalization) and intensity normalization (z-score, min-max scaling, histogram standardization, and intensity clipping). Several top teams leveraged the automated preprocessing pipeline of the nnU-Net framework (Isensee et al., 2022). Postprocessing was less commonly applied but was utilized by four teams to refine predictions. Such techniques included selecting the largest connected component for each anatomical structure (either slice-wise or volume-wise) or employing the postprocessing pipeline provided by nnU-Net.

6.5.4. Data augmentation

Extensive data augmentation was a universal feature of the submitted methods. In addition to standard spatial and intensity-based transformations, many teams implemented augmentations specifically designed to simulate motion artifacts. These included k-space-based artifact simulation and adversarial augmentation techniques like AdvChain (Chen et al., 2022), where the model is trained to be robust against worst-case perturbations. Test-Time Augmentation (TTA) was also employed by some teams to improve the robustness of the final predictions.

6.6. Details of RCS algorithms

6.6.1. S1. UA-SVCC

UA-SVCC (Mora-Rubio et al., 2022) employed a modified version of the nnU-Net framework (Isensee et al., 2021), which has previously demonstrated strong performance in CMR segmentation challenges. The authors utilized the official nnU-Net implementation (Isensee et al., 2022) to handle preprocessing tasks such as resampling, normalization, patch size configuration, and the adjustment of training hyperparameters (e.g., batch size). These parameters were tailored according to the characteristics of the input data and the available computational resources.

This method adopted a multi-stage training strategy. In the initial stage, only the cross-entropy loss was used. In

the second stage, both cross-entropy and Dice losses were combined. In the final stage, only the Dice loss was employed. This progression allows the network to first prioritize accurate class distribution (via cross-entropy loss) and then refine the spatial alignment of segmentation regions (via Dice loss). As a result of this training strategy, the method achieved state-of-the-art performance on Task 2 during the testing phase.

6.6.2. S2. Med-Air

Team Med-Air tied for first place in Task 2 due to its comparable performance with S1.UA-SVCC in the final rankings (see Section 6.8.2). This approach proposed a comprehensive ensemble framework that integrated multiple architectures, including 2D nnU-Net, 3D nnU-Net, Swin-UNETR (Hatamizadeh et al., 2022), and Swin-UNet (Cao et al., 2023), together with a diverse collection of publicly available datasets used as external resources.

For the transformer-based models, the encoder of Swin-UNETR was pretrained using four external datasets (SCD (Radau et al., 2009), RVSC (Petitjean et al., 2015), LASB’13 (Tobon-Gomez et al., 2015), and ADSB (A. et al., 2015)) via multi-task self-supervised learning methods (Tang et al., 2022). The encoder of Swin-UNet was pretrained on ImageNet (Deng et al., 2009). Subsequently, all candidate models were further pretrained on publicly available cardiac segmentation datasets, including ACDC (Bernard et al., 2018), M&Ms-1 (Campello et al., 2021), M&Ms-2 (Martín-Isla et al., 2023), MyoPS (Zhuang, 2019), and MS-CMRSeg (Zhuang, 2016). To enhance the model’s robustness to diffeomorphic deformations and spatial transformations, the AdvChain framework (Chen et al., 2022) was employed in conjunction with random data augmentation in an iterative training scheme.

These four network architectures, incorporating both pretraining and adversarial augmentations, were trained under a 5-fold cross-validation setting on the training set to produce the average ensemble prediction. Evaluation on the validation dataset demonstrated that pretraining led to notable improvements in the segmentation accuracy of the LV and MYO, while AdvChain contributed substantial performance gains for the RV. As a result, this approach achieved first place and yielded the best DSC scores for the MYO and RV regions.

6.6.3. S3. CMR.Love.LHND

CMR.Love.LHND(Yang et al., 2022) ranked second in Task 2 and investigated the use of two different network architectures. Initially, they employed a combination of a bidirectional convolutional LSTM (Bi-ConvLSTM) (Bai et al., 2020) and a 2D U-Net, inspired by previous research (Zhang et al., 2018) which demonstrated that recurrent neural networks (RNNs) can capture features across consecutive frames of the cardiac cycle, potentially improving segmentation performance by leveraging spatial continuity along the slice dimension. After comparing the performance of Bi-ConvLSTM and nnU-Net, they ultimately adopted the nnU-Net framework, which integrates both 2D and 3D models in an ensemble configuration. This network was further enhanced by extensive data augmentation

strategies, including aggressive Gaussian noise, Gaussian blur, and modifications to brightness, contrast, and gamma correction. This comprehensive setup contributed to the model’s robustness and obtained a second-place ranking on the testing set.

6.6.4. *S4. Tewodros*

Tewodros (Arega et al., 2022) also tied for second place and employed nnU-Net as the baseline segmentation network. This approach proposed a moderate k-space-based motion artifact augmentation strategy and introduced a hybrid loss function, termed DicePolyCE loss, which combines a region-based Dice loss with a polynomial variant of the cross-entropy loss. This design enhances segmentation performance and improves the model’s generalization capability for cardiac MR segmentation under motion artifact conditions.

The augmentation strategy used in this method was categorized into three levels: light augmentation, moderate motion artifact augmentation (moderate MAA), and heavy motion artifact augmentation (heavy MAA). These levels were defined based on the number of simulated motion artifacts generated using the TorchIO library (Pérez-García et al., 2021). Extensive experiments demonstrated that moderate MAA achieved the best performance, whereas light augmentation yielded suboptimal results, and heavy MAA led to excessive image distortion. Additionally, k-space motion artifacts were applied to randomly selected high-quality training images. These synthesized images, combined with supplementary data from the external ACDC dataset (Bernard et al., 2018), were incorporated into the training set to enhance sample diversity. This strategy further improved segmentation performance, contributing to the method’s second-place ranking in Task 2.

6.6.5. *S5. OpenGTN*

Team OpenGTN (Amirrajab et al., 2022) secured third place in Task 2 by developing an ensemble framework based on modified 2D nnU-Net models tailored to address data variability and the segmentation challenges of the basal and apical heart regions, particularly under motion artifacts. To augment the training dataset with motion artifact, respiratory motion is simulated by applying sinusoidal translations to artifact-free images before transforming them into the Fourier domain, allowing adjustment of artifact severity via parameters controlling the period and amplitude of the motion, the method incorporated two external datasets, namely M&Ms-1 (Campello et al., 2021) and M&Ms-2 (Martín-Isla et al., 2023).

The final heart cavity segmentation was generated by ensembling predictions from three distinct training strategies: (1) training a 2D nnU-Net on the full dataset with simulated motion artifacts, (2) training another model using non-homogeneous batch sampling, and (3) combining three region-specific models specialized for the basal, mid-ventricular, and apical slices.

To address the segmentation difficulty in basal and apical slices, especially in the presence of motion artifact, the non-homogeneous batch sampling method was employed to oversample these critical slices within each mini-batch.

Moreover, Focal-Tversky loss (Abraham and Khan, 2019) was utilized for region-specific training of the apical and basal areas, focusing on better boundary delineation and class imbalance. These strategies collectively led to improved segmentation performance across all cardiac regions and enabled the team to achieve third place in the final rankings.

6.6.6. *S6. Abdul*

Abdul (Qayyum et al., 2022) proposed a two-stage segmentation framework to enhance performance through a combination of generalization and pseudo-label supervision. In the first stage, a 3D-ResUNet was employed, incorporating lightweight 3D convolutional blocks in the encoder, residual modules (He et al., 2016) in the skip connections, and a three-level deep supervision mechanism (Lee et al., 2015). This network generated pseudo labels on the validation set using an ensemble of models trained via cross-validation. In the second stage, an nnU-Net was trained using both the pseudo labels and original training data. The 3D-ResUNet architecture featured an encoder-decoder structure with residual blocks, 3D strided convolutions for spatial downsampling, and 3D transposed convolutions for upsampling. Feature maps from the encoder were concatenated with those in the decoder to preserve semantic context, while deep supervision guided the network by computing aggregated losses at multiple levels. The modified nnU-Net was trained with a batch size of $96 \times 160 \times 160$ over 500 epochs using one-fold cross-validation.

6.6.7. *S7. Philips_CTS*

Team Philips_CTS (Li et al., 2022) adopted the 2D nnU-Net as the backbone architecture, which was deemed more suitable due to the relatively large slice thickness in the dataset. To improve the segmentation performance, particularly for small anatomical structures, the team proposed a sequential, cascaded two-stage segmentation framework.

In the first stage, a nnU-Net was trained to predict a binary mask encompassing all three structures (i.e., LV, MYO, and RV). Based on this output, new input images were generated by zeroing out the pixels outside the binary mask. These masked images, along with the original three-class labels, were then used to train a second model. The input to the second-stage model was obtained by multiplying the original image by the binary mask from the first stage, and the output consisted of three separate masks corresponding to the target structures.

To mitigate data scarcity and leverage additional information from unlabeled data, the model was further trained using pseudo labels derived from unlabeled samples. This strategy enhanced the model’s performance on the validation set, ultimately securing 5th place in Task 2.

6.6.8. *S8. MI-IST_DA*

Team MI-IST_DA (Ranem et al., 2022b) adopted a 2D ViT U-Net V2 framework (Ranem et al., 2022a), derived from the Lifelong nnU-Net (González et al., 2023) and based on a Vision Transformer (Dosovitskiy et al., 2020) backbone, for cardiac segmentation. This architecture was chosen after a comparative evaluation against nnU-Net models

in both 2D and 3D configurations, where ViT U-Net demonstrated the highest scores across all segmentation labels and superior robustness to motion artefacts. Visualization analyses further showed that ViT U-Net generated more complete segmentations of the MYO and LV compared to 2D and 3D nnU-Net models in local evaluations, supporting the hypothesis that the self-attention mechanism of Transformers allows the model to focus more effectively on cardiac structures under motion artefacts. For the final submission, an ensemble of three models – namely 2D ViT U-Net, 2D nnU-Net, and 3D nnU-Net – was used to combine their complementary strengths. Enhanced by the dynamic preprocessing and postprocessing pipeline of nnU-Net, this ensemble ultimately ranked 6_{th} in Task 2.

6.6.9. S9. HAHA2

Team HAHA2 (Ma et al., 2022) developed a semi-supervised segmentation framework called Confidence-Aware Cross Pseudo Supervision (CACPS), based on a semi-supervised domain generalization strategy (Yao et al., 2022), to improve the quality of pseudo labels. This approach treats different respiratory motions as distinct image domains and employs Fourier transformation for data augmentation. Specifically, paired images from the source domain are randomly sampled and transformed into the frequency domain via Fourier transformation. A weighted combination of their amplitude spectra, together with phase information from one of the images, is then computed to synthesize new training images. These generated and the original images are fed into a dual-path confidence-aware cross pseudo supervision network inspired by (Chen et al., 2021), with DeepLabV3+ (Chen et al., 2017) as the backbone. The proposed CACPS framework outperformed the baseline DeepLabV3+, and further improvements were observed by ensembling two CACPS networks with different backbones (i.e., DeepLabV3+ and ResNet-101).

6.6.10. S10. ML-Labs

Team ML-Labs (Garcia-Cabrera et al., 2022) implemented a ResNet-based U-Net (Ronneberger et al., 2015) architecture that employs ResNet-101 (He et al., 2016) as the encoder, with weights pre-trained on the ImageNet classification task. The approach integrates four effective data augmentation techniques to enhance robustness. These techniques include random motion simulation following the method in (Shaw et al., 2019), random ghosting to simulate the effect along the phase-encoded direction, and altering the intensity of imaged structures. It also employs random bias field transformation to introduce low-frequency intensity inhomogeneity, modeled as a linear combination of polynomial functions (as described in (Van Leemput et al., 1999)), and random gamma transformation to adjust image contrast by raising pixel values to a random power. Extended experiments demonstrated that tripling the intensity of random motion augmentation, compared to the other techniques, results in a model that is more resilient to respiratory motion artifacts, thereby improving segmentation performance.

6.6.11. S11. Sano

Team Sano (Grzeszczyk et al., 2022) proposed a multi-task learning framework that concurrently performs motion

artifact classification and CMR segmentation in a single forward pass. Their approach is based on a modified multi-task architecture inspired by Swin UNETR (Swin U-Net Transformers), following the design introduced by (Hatamizadeh et al., 2022). In this framework, segmentation is treated as the primary task, while IQA serves as an auxiliary task. The final prediction is obtained through an ensemble of five networks trained using 5-fold stratified cross-validation. Stratification is performed based on the classification labels to ensure an even distribution of motion artifacts across all folds. This method achieved competitive results in terms of DSC and HD95.

6.6.12. S12. sots

Team SOTS (Kou et al., 2022) also proposed a multi-task learning framework that integrates DenseBiasNet (He et al., 2020) with a Variational Auto-Encoder (VAE) inspired by (Myronenko, 2019). In this framework, DenseBiasNet serves as the primary branch for segmentation, while the VAE functions as an auxiliary branch to enhance representation learning.

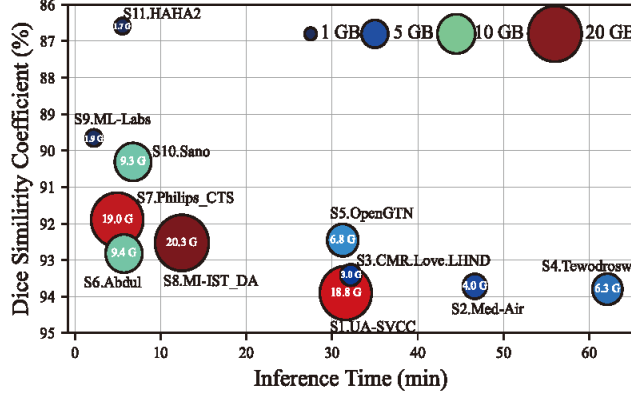
A shared encoder with dense bias connections from DenseBiasNet is employed to fuse multi-scale and multi-receptive field features, providing rich contextual representations for both segmentation and reconstruction tasks. The VAE takes as input a low-resolution image derived from the encoder output of DenseBiasNet and maps it to a low-dimensional latent space to reconstruct the original image. The segmentation task is supervised using a combination of Soft Dice loss (Milletari et al., 2016) and cross-entropy loss, whereas the reconstruction task is guided by an L2 loss.

Collaborative training of the VAE and DenseBiasNet branches yields improved segmentation performance compared to using DenseBiasNet alone. Notably, local validation results indicate that as the severity of respiratory motion artifacts increases, the segmentation quality of both the LV and MYO becomes more dominant, suggesting enhanced robustness under artifact-heavy conditions.

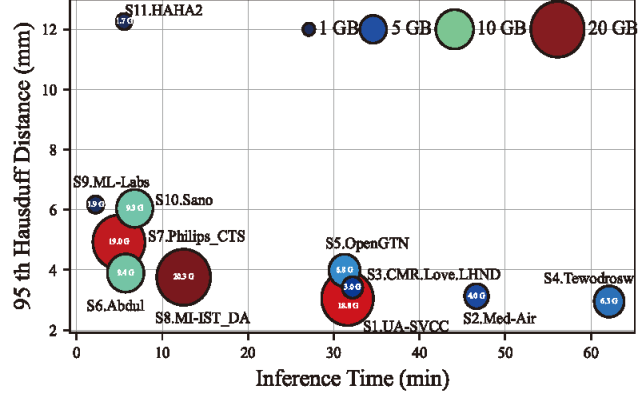
6.7. Computational efficiency analysis

Beyond segmentation accuracy, the computational efficiency of the algorithms is a critical factor for their potential clinical translation. We evaluated the inference time and peak GPU memory usage of all submitted Docker containers on a standardized hardware platform. The results are summarized in Table 9 and Table 10.

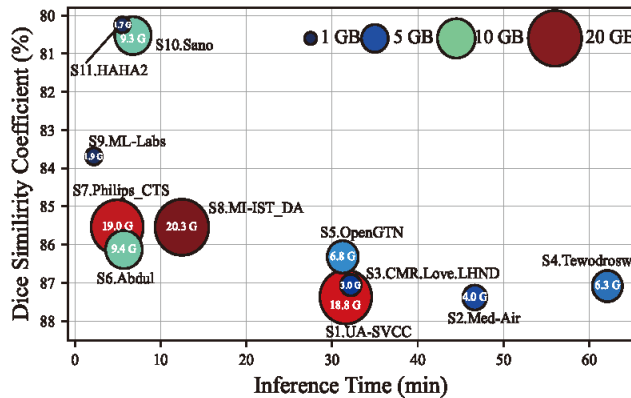
Table 9: The computation consumption for the IQA task on the testing set. The **Max VRAM** represents the allocated peak GPU VRAM, and the **Inference time** is the total processing time, which includes data loading, pre-processing, model inference, post-processing, and data saving. These measurements were taken using 120 testing images during the testing phase on our testing platform. None represents the algorithm is specified running in cpu mode.



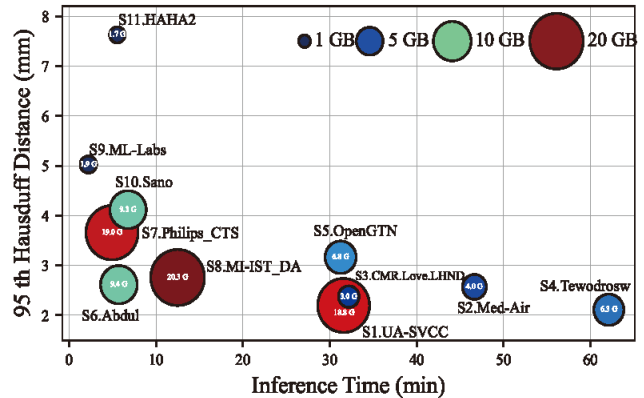
(a) Computational Consumption vs. DSC_{LV}



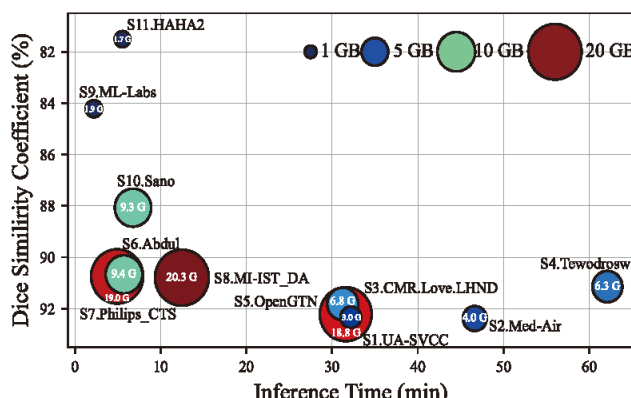
(b) Computational Consumption vs. $HD95_{LV}$



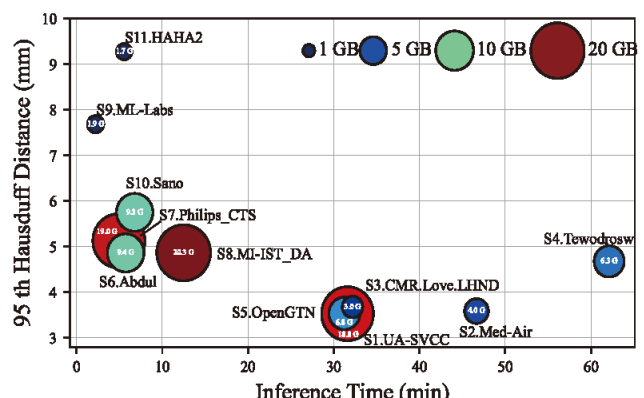
(c) Computational Consumption vs. DSC_{MYO}



(d) Computational Consumption vs. $HD95_{MYO}$

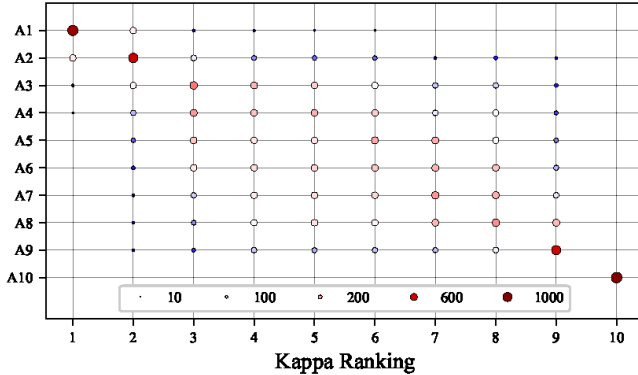


(e) Computational Consumption vs. DSC_{RV}

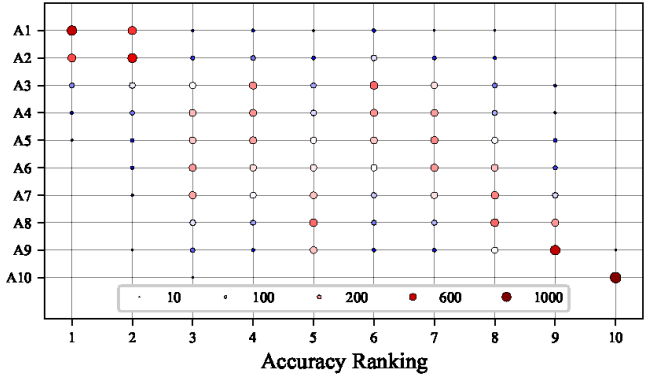


(f) Computational Consumption vs. $HD95_{RV}$

Figure 9: Analysis of computational efficiency versus segmentation performance for the top 10 teams in the RCS task. The x-axis of each plot represents the total inference time, while the y-axis represents the segmentation metric (DSC or HD95) for the LV, MYO, and RV. The size of each data point corresponds to the peak GPU VRAM usage.



(a) Bootstrap ranking frequency of Cohen's Kappa



(b) Bootstrap ranking frequency of Accuracy

Figure 10: Matrix bubble chart of ranking statistics for IQA task (Task 1) based on 1,000 bootstrap samples. (a) the bootstrap ranking frequencies for Cohen's Kappa, while (b) the bootstrap ranking frequencies for Accuracy. In this visualization, the area of each data node indicates its ranking frequency across the 1,000 bootstrap samples. The corresponding color is assigned using a value-based colormap that resembles the seismic colormap.

TID	Team Name	Max VRAM	Inference Time
A1	UON_IMA	2.46 GB	11.94 min
A2	Philips_CTS	19.08 GB	14.98 min
A3	OpenGTN	-	10.12 min
A4	issun	4.41 GB	78.44 min
A5	Tewodros	1.77 GB	1.33 min
A6	CMR.Love.LHND	1.58 GB	1.78 min
A7	MI-IST_DA	20.33 GB	12.36 min
A8	UA-SVCC	2.49 GB	0.45 min
A9	Abdul	2.99 GB	1.17 min
A10	Sano	9.31 GB	6.06 min

For the RCS task, the total inference time for the 120 test cases ranged from 1.19 to 62.12 minutes, with peak GPU VRAM consumption ranging from 1.69 GB to 20.27 GB. As illustrated in Fig. 9, there was a clear trade-off between performance and efficiency. The top-ranked algorithms from UA-SVCC and Med-Air, while achieving the highest accuracy, were also among the more computationally intensive solutions. Conversely, algorithms that prioritized faster inference often did so at the cost of segmentation accuracy. These results highlight the ongoing challenge of developing models that are both highly accurate and computationally efficient enough for seamless integration into clinical workflows.

Table 10: The computation consumption for the segmentation task on the testing set. The **Max VRAM** represents the peak allocated GPU VRAM, and the **Inference time** is the total processing time, which includes data loading, preprocessing, model inference, post-processing, and data saving. These measurements were taken using 120 testing images during the testing phase on our testing platform.

TID	Team Name	Max VRAM	Inference Time
S1	UA-SVCC	18.81 GB	31.60 min
S2	Med-Air	4.01 GB	46.65 min
S3	CMR.Love.LHND	2.98 GB	32.19 min
S4	Tewodros	6.32 GB	62.12 min
S5	OpenGTN	6.80 GB	31.25 min
S6	Abdul	9.41 GB	5.73 min
S7	Philips_CTS	19.02 GB	4.94 min
S8	MI-IST_DA	20.27 GB	12.49 min
S9	ML-Labs	1.90 GB	2.22 min
S10	Sano	9.31 GB	6.78 min
S11	HAHA2	1.69 GB	5.55 min
S12	sots	6.06 GB	1.19 min

6.8. Ranking analysis

6.8.1. Ranking of IQA task

The final ranking for the IQA task was determined by the linearly weighted Cohen's Kappa coefficient, a metric chosen for its robustness to class imbalance compared to standard accuracy. As reported in Table. 6, submissions were sorted in descending order based on their Kappa score on the held-out test set. To evaluate the stability of this ranking, we performed a bootstrap analysis (1,000 samples) for both the Kappa and accuracy metrics. The results, visualized in Fig. 10, demonstrate that Kappa provides a more stable and reliable ranking. The ranking frequency distribution for Kappa is highly concentrated along the main diagonal, indicating that the top-performing teams consistently maintained their high ranks across the bootstrap samples. In contrast, the ranking distribution based on accuracy was significantly more dispersed, with greater variance and a higher degree of randomness, reinforcing the choice of Kappa as the primary evaluation metric.

6.8.2. Ranking of RCS task

For the RCS task, we employed a robust *rank-then-aggregate* strategy to determine the final standings. This approach ensures that the final ranking reflects consistent performance across all evaluation criteria, rather than being skewed by exceptional performance on a single metric or structure. For each of the 120 test cases, every participating team was ranked based on six individual metrics: the Dice Similarity Coefficient (DSC) and the 95% Hausdorff Distance (HD95) for each of the three anatomical structures (LV, MYO, and RV). The final ranking score for each team was then calculated as the mean of these individual ranks across all test cases. To determine if the differences between the final ranking scores were statistically significant, we performed pairwise comparisons using the two-sided Wilcoxon signed-rank test, with p-values corrected for multiple comparisons using the Holm-Bonferroni procedure. As shown in the significance matrix in Fig. 11, this analysis revealed no significant difference between the top two teams (S1.UA-SVCC and S2.Med-Air), resulting in a tie for first place. Similarly, teams S3.CMR.Love.LHND and S4.Tewodros were found to have statistically comparable performance, resulting in a tie for second place.

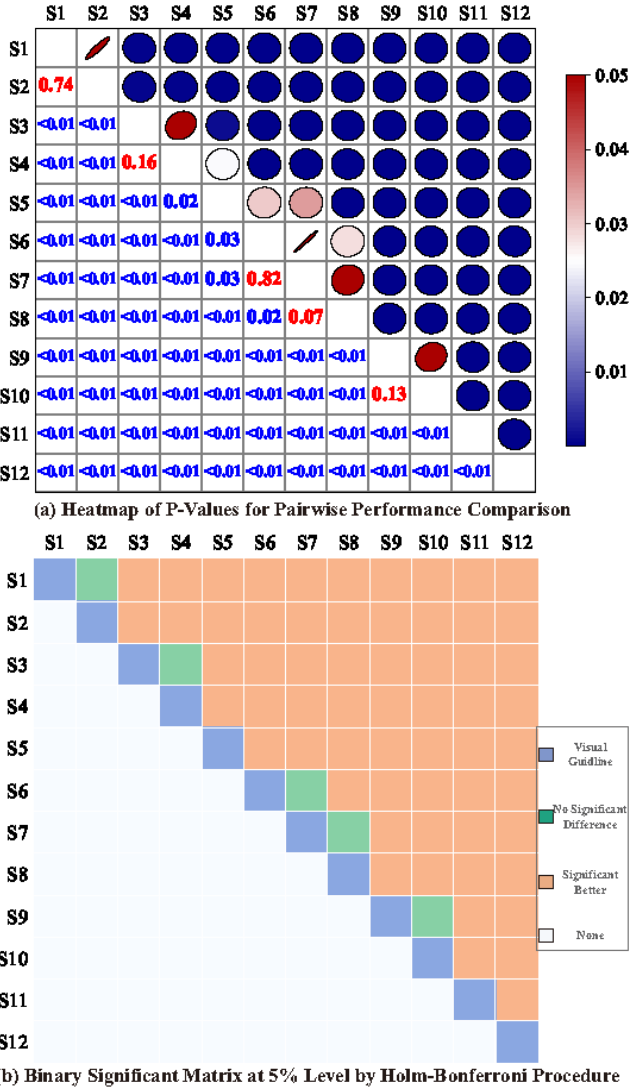


Figure 11: Statistical analysis of the RCS ranking. (a) p-value heatmap from the pairwise Wilcoxon signed-rank tests. The shrinkage of each ellipse corresponds to the p-value. (b) binary significance matrix at the 5% level after Holm-Bonferroni correction. Orange indicates the row significantly outperformed the column, while cyan indicates no significant difference.

7. Discussion

This challenge was designed to establish the first benchmark for assessing the impact of respiratory motion on CMR image quality and the robustness of automated segmentation models. In this section, we analyze the performance of the submitted algorithms, contextualize the results, and discuss the implications for future research. In particular, we further investigate the downstream effects of motion artifacts on clinical imaging biomarkers, and compare the top-performing algorithms against human expert performance.

7.1. Performance on the IQA task

The challenge results demonstrate that automated IQA is a feasible but challenging task. The top-performing algorithm achieved a Cohen’s Kappa score of 0.631, indicating a good level of agreement with the expert radiologists’ assessment. This level of performance suggests that automated tools could be reliably used to flag images with motion artifacts in a clinical workflow.

However, the overall performance landscape reveals significant room for improvement. While the winning method showed a high level of consistency, the majority of submitted algorithms achieved only moderate agreement (Kappa scores between 0.41 and 0.60), and no method reached an excellent level of agreement ($\kappa > 0.80$). A key finding, illustrated by the confusion matrixes in Fig. 3, is that while most algorithms could effectively identify high-quality images (mild motion), they struggled to accurately classify the severity of motion in more degraded images. This indicates that while current models are promising for binary quality control (i.e., usable vs. unusable), fine-grained assessment of artifact severity remains an open research problem.

7.2. Performance on the RCS task

For the RCS task, the state-of-the-art deep learning models demonstrated high accuracy on the test set, with the best average DSC scores reaching 93.90% for the LV, 87.38% for the MYO, and 92.39% for the RV. Consistent with previous segmentation challenges, the MYO proved to be the most difficult structure to segment due to its thin anatomy, resulting in lower DSC scores despite often achieving good surface distance metrics (HD95).

7.2.1. The impact of motion artifacts on segmentation and clinical imaging biomarkers

A central goal of this challenge was to quantify the impact of motion artifacts on segmentation performance. Our subgroup analysis, presented in Table. 11, confirms a clear trend: as image quality degrades (i.e., as the IQA score increases), the segmentation accuracy of all top-performing algorithms decreases. For example, the DSC for LV segmentation for the top-ranked algorithm dropped by over 3 percentage points between the best- and worst-quality images.

This degradation in segmentation accuracy has a direct, clinically significant downstream effect. As shown in the Bland-Altman plots in Fig. 12 and the detailed error analysis in Tables. 12 to 16, the error in derived clinical biomarkers, such as ejection fraction and ventricular volumes, increases substantially as image quality worsens. For instance, the Mean Absolute Error (MAE) for the LV end-diastolic volume (LV_{EDV}) more than doubled for the top algorithm when comparing images with mild versus severe motion artifacts as shown in Fig. 13. This finding underscores the critical importance of developing motion-robust segmentation models, as even subtle segmentation inaccuracies in degraded images can lead to significant errors in the clinical parameters used for diagnosis and patient management.

7.2.2. Comparison with human expert performance

To contextualize the performance of the automated methods, we conducted an inter-observer validation study. The error analysis of five derived clinical biomarkers calculated from the annotations of human experts are shown in Fig. 16 and Table. 18, as well as the detailed Bland-Altman plots shown in Fig. 16. The results, summarized in Table. 17 and Fig. 14, reveal that the top-performing AI algorithms are approaching the level of human experts for segmenting the LV and MYO in images with mild to intermediate motion

Table 11: Subgroup analysis of segmentation performance for top 3 methods under different IQA scores. The reported data are in the format of mean \pm standard deviation. \uparrow represents higher is better, \downarrow represents lower is better. Bold represent the best performance of corresponding IQA score.

IQA Score	Methods	DSC (%) \uparrow			HD95 (mm) \downarrow		
		LV	MYO	RV	LV	MYO	RV
1	S1. UA-SVCC	94.63 \pm 3.27	87.82 \pm 4.17	93.14 \pm 5.59	2.52 \pm 3.19	2.27 \pm 2.50	2.95 \pm 3.21
	S2. Med-Air	94.49 \pm 4.04	88.10 \pm 3.71	93.20 \pm 5.53	2.65 \pm 3.57	2.51 \pm 2.92	3.07 \pm 3.95
	S3. CMR.Love.LHND	94.22 \pm 3.47	87.57 \pm 4.26	93.45 \pm 3.82	2.96 \pm 3.58	2.31 \pm 2.49	2.82 \pm 2.83
	S4. Tewodros	94.35 \pm 3.53	87.73 \pm 3.84	92.16 \pm 5.48	2.75 \pm 3.41	2.02 \pm 1.85	4.22 \pm 3.84
	S5. OpenGTN	93.10 \pm 5.18	86.95 \pm 3.69	92.44 \pm 5.64	3.73 \pm 4.53	3.09 \pm 3.23	3.17 \pm 3.04
2	S1. UA-SVCC	93.21 \pm 3.95	86.94 \pm 2.40	91.33 \pm 6.36	3.55 \pm 3.77	2.15 \pm 1.69	4.08 \pm 3.76
	S2. Med-Air	92.98 \pm 4.44	86.72 \pm 2.65	91.59 \pm 5.43	3.58 \pm 3.80	2.65 \pm 2.50	4.10 \pm 3.71
	S3. CMR.Love.LHND	92.63 \pm 4.45	86.56 \pm 2.75	91.28 \pm 4.60	3.87 \pm 3.84	2.45 \pm 2.06	4.49 \pm 3.67
	S4. Tewodros	93.26 \pm 3.91	86.49 \pm 2.40	90.16 \pm 6.17	3.17 \pm 3.38	2.21 \pm 1.72	5.15 \pm 4.14
	S5. OpenGTN	91.81 \pm 6.01	85.70 \pm 3.22	91.19 \pm 6.06	4.27 \pm 4.36	3.27 \pm 3.14	3.91 \pm 3.59
3	S1. UA-SVCC	91.76 \pm 5.05	83.12 \pm 6.49	87.25 \pm 6.21	3.95 \pm 4.21	4.62 \pm 4.84	7.45 \pm 5.69
	S2. Med-Air	91.01 \pm 5.72	82.85 \pm 6.09	87.97 \pm 6.66	4.86 \pm 5.55	5.06 \pm 5.40	6.84 \pm 5.77
	S3. CMR.Love.LHND	91.23 \pm 5.01	82.07 \pm 6.59	87.63 \pm 5.77	4.56 \pm 4.28	5.00 \pm 4.77	6.39 \pm 4.38
	S4. Tewodros	91.57 \pm 4.78	83.09 \pm 6.26	88.49 \pm 5.55	3.94 \pm 3.54	3.54 \pm 2.73	5.75 \pm 4.83
	S5. OpenGTN	90.68 \pm 5.51	81.74 \pm 5.72	89.03 \pm 5.13	4.35 \pm 3.51	4.45 \pm 3.24	5.42 \pm 3.59

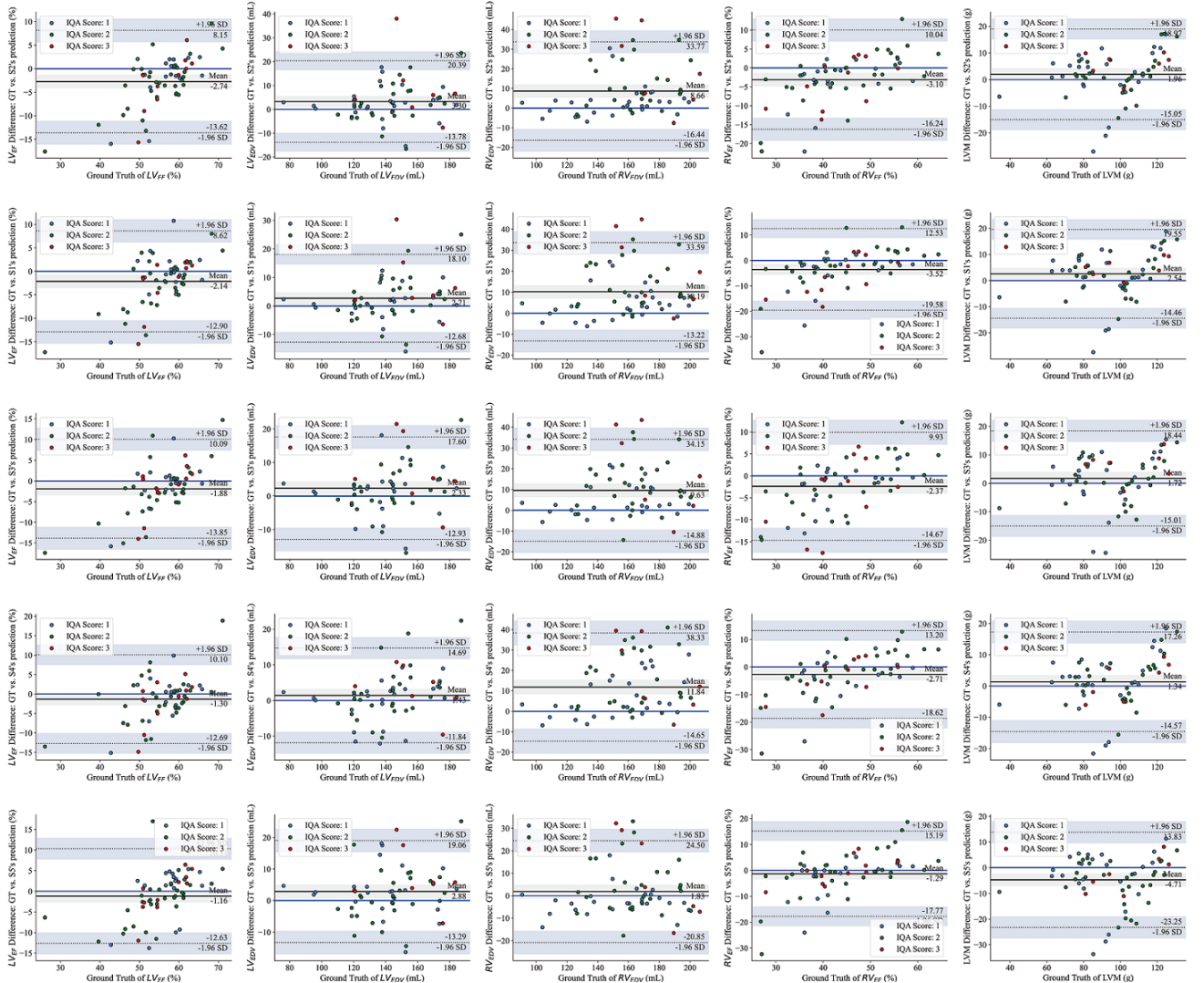


Figure 12: Bland-Altman plots illustrating the agreement between AI-derived and ground-truth clinical biomarkers for the top five RCS algorithms. Each row corresponds to an algorithm, and each column represents a different clinical biomarker: (a) LV_{EF} , (b) RV_{EF} , (c) LV_{EDV} , (d) LVM , and (e) RV_{EDV} . The solid black line indicates the mean difference, and the dashed lines represent the 95% limits of agreement.

Table 12: Differences between clinical indicators predicted by S1 and the gold standard across different IQA score levels.

Metrics	IQA 1		IQA 2		IQA 3	
	MAE	RMSE	MAE	RMSE	MAE	RMSE
LV_{EDV} (mL)	4.51	6.12	5.84	8.26	9.55	13.43
LV_{EF} (%)	3.14	4.85	4.77	6.29	3.93	6.16
RV_{EDV} (mL)	6.69	9.08	12.68	16.43	22.10	27.28
RV_{EF} (%)	4.67	7.85	5.91	9.15	7.79	9.65
LVM (g)	8.23	10.70	6.53	8.11	6.24	7.88

Table 13: Differences between clinical indicators predicted by S2 and the gold standard across different IQA score levels.

Metrics	IQA 1		IQA 2		IQA 3	
	MAE	RMSE	MAE	RMSE	MAE	RMSE
LV_{EDV} (mL)	5.40	7.31	6.30	8.61	10.78	15.82
LV_{EF} (%)	3.30	5.50	4.85	6.49	4.36	6.25
RV_{EDV} (mL)	5.93	9.17	11.47	15.51	22.67	28.04
RV_{EF} (%)	4.39	7.22	5.32	7.46	5.53	7.20
LVM (g)	7.57	10.28	6.10	8.06	6.68	8.08

Table 14: Differences between clinical indicators predicted by S3 and the gold standard across different IQA score levels.

Metrics	IQA 1			IQA 2			IQA 3			Metrics	IQA 1			IQA 2			IQA 3			Metrics	IQA 1			IQA 2			IQA 3														
	MAE	RMSE	MAE	RMSE	MAE	RMSE	MAE	RMSE	MAE	RMSE	MAE	RMSE	MAE	RMSE	MAE	RMSE	MAE	RMSE	MAE	RMSE																					
LV_{EDV} (mL)	5.19	6.75	5.78	7.99	9.40	11.94	LV_{EDV} (mL)	4.44	5.80	5.29	7.70	5.88	7.07	LV_{EDV} (mL)	6.02	7.94	6.12	8.44	9.37	11.68	LV_{EF} (%)	3.11	4.96	5.47	7.19	4.07	5.99	LV_{EF} (%)	4.72	6.08	4.41	6.12	4.06	5.01							
LV_{EF} (%)	3.11	4.96	5.47	7.19	4.07	5.99	LV_{EF} (%)	3.43	5.00	4.54	6.38	4.10	6.03	LV_{EF} (%)	4.72	6.08	4.41	6.12	4.06	5.01	RV_{EDV} (mL)	6.32	8.83	13.63	16.92	21.60	26.85	RV_{EDV} (mL)	9.53	12.74	14.92	19.96	19.52	24.56	RV_{EDV} (mL)	4.86	6.53	9.20	12.47	16.69	19.97
RV_{EDV} (mL)	6.32	8.83	13.63	16.92	21.60	26.85	RV_{EF} (%)	5.14	8.01	6.56	9.01	5.67	7.83	RV_{EF} (%)	4.95	8.15	6.25	9.55	4.03	4.99	LVM (g)	7.70	10.27	5.70	7.32	8.19	8.87	LVM (g)	6.94	9.47	5.92	7.50	6.09	7.44	LVM (g)	8.12	12.07	6.53	8.84	8.97	11.68
RV_{EF} (%)	3.78	5.46	5.04	6.46	6.59	8.75	LVM (g)	12.11	9.52	10.64	12.11	9.52	10.64	LVM (g)	11.34	8.73	10.18	11.34	8.73	10.18	LVM (g)	3.17	4.45	5.95	4.85	6.12	7.85	LVM (g)	3.83	5.50	5.50	5.50	5.50	5.50	LVM (g)	3.83	5.50	5.50	5.50	5.50	5.50

Table 15: Differences between clinical indicators predicted by S4 and the gold standard across different IQA score levels.

Table 16: Differences between clinical indicators predicted by S5 and the gold standard across different IQA score levels.

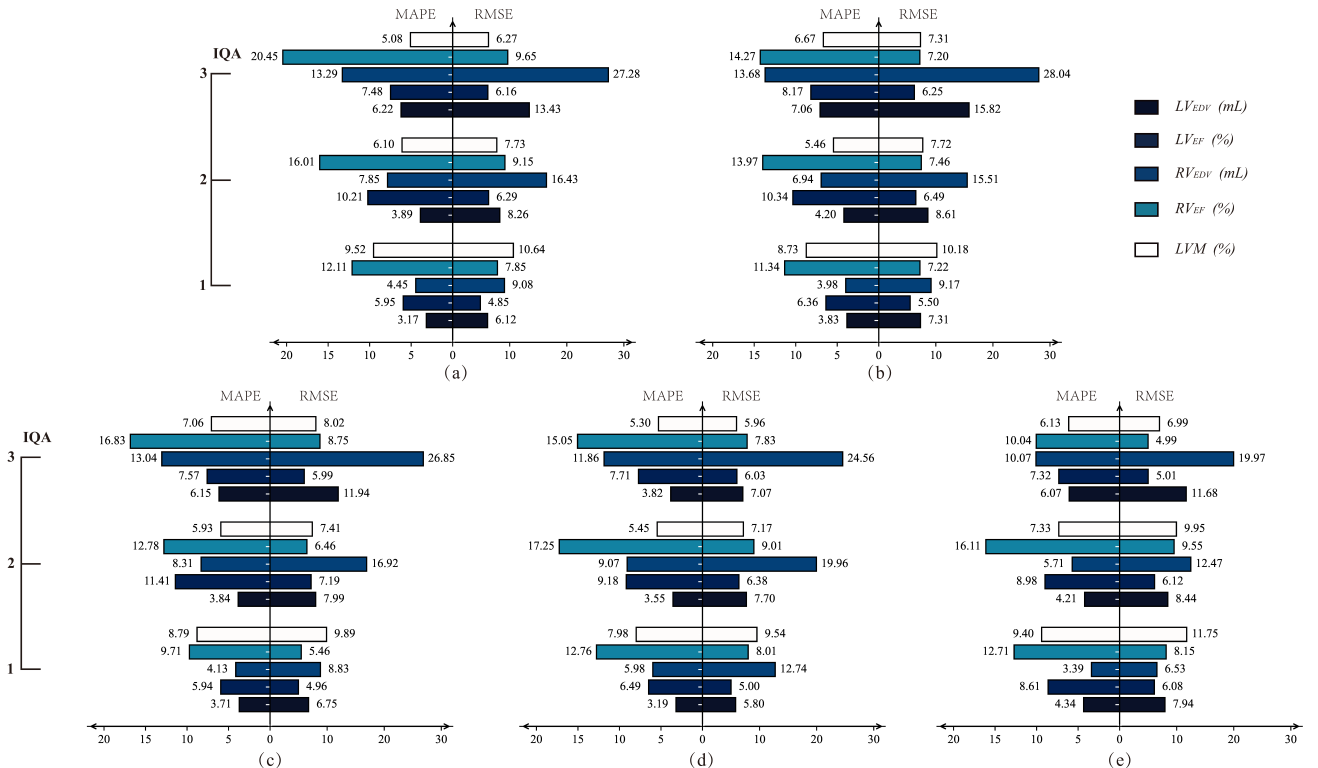


Figure 13: Bidirectional bar charts showing the error in clinical biomarkers for the top five RCS algorithms, stratified by IQA score. The left bars represent the Mean Absolute Percentage Error (MAPE), and the right bars represent the Root Mean Square Error (RMSE).

artifacts. For these structures, there was no statistically significant difference between the best AI model and the expert annotator.

However, a performance gap remains, particularly for the RV and in images with severe artifacts. Human experts consistently outperformed the AI models in RV segmentation across all quality levels and demonstrated greater robustness in segmenting all structures in severely degraded images. This suggests that while AI is nearing human-level performance under ideal conditions, improving robustness to severe artifacts and mastering the complex geometry of the RV are key areas for future work.

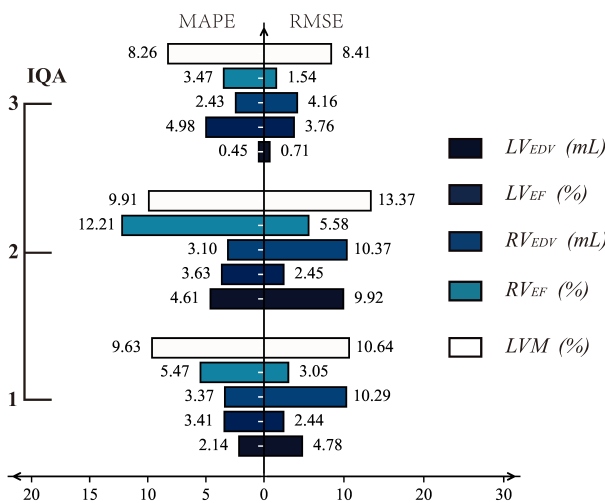


Figure 16: Bidirectional bar chart of clinical indicator errors between two human observers, stratified by IQA score. The left bars show the MAPE, and the right bars show the RMSE.

Table 18: Differences of clinical indicators between independent observers.

Metrics	IQA 1		IQA 2		IQA 3	
	MAE	RMSE	MAE	RMSE	MAE	RMSE
LV_{EDV} (mL)	2.91	4.78	7.01	9.92	0.71	0.71
LV_{EF} (%)	2.00	2.44	2.08	2.45	2.91	3.76
RV_{EDV} (mL)	5.76	10.29	5.16	10.37	4.16	4.16
RV_{EF} (%)	2.31	3.05	4.91	5.58	1.38	1.54
LVM (g)	9.19	10.64	11.18	13.37	8.41	8.41

7.3. Limitations and future directions

The *CMRxMotion* challenge has provided a valuable benchmark, but it also highlights several limitations and opportunities for future research.

Advancing model architectures: The top-performing solutions in this challenge primarily relied on established architectures like nnU-Net and EfficientNet. Future work could explore the potential of newer architectures, such as Vision Foundation Models, which may offer enhanced feature representation capabilities. Furthermore, the exploration of more sophisticated multi-task and self-supervised learning frameworks could lead to improved generalization and robustness.

Clinical translation and efficiency: A significant barrier to the clinical adoption of many of the submitted algorithms is their computational cost. As shown in our efficiency analysis (Fig. 9), the most accurate models were

often the most computationally intensive. Future research should focus on model optimization and the development of lightweight architectures that can provide rapid inference without sacrificing accuracy, a prerequisite for real-time clinical applications.

Synergy with image reconstruction: This challenge focused on analyzing already-acquired images. A promising future direction is the synergistic development of segmentation algorithms and accelerated, motion-corrected MRI reconstruction techniques. By improving the quality of the input images at the source, the challenge of robust segmentation could be substantially mitigated.

Dataset diversity: The challenge dataset, while carefully curated, was based on simulated motion from healthy volunteers at a single center. To develop truly generalizable models, future efforts should focus on collecting large-scale, multi-center datasets that include real-world clinical data from diverse patient populations with a wide range of pathologies. This will be essential for training and validating models that are robust to the full spectrum of challenges encountered in routine clinical practice.

8. Conclusion

The *CMRxMotion* challenge established the first public benchmark for evaluating the robustness of automated CMR analysis algorithms against respiratory motion artifacts. Through a unique dataset with a controlled spectrum of motion, we provided a standardized framework for assessing automated image quality assessment and robust cardiac segmentation.

The results from 22 submitted algorithms demonstrate that while automated IQA is feasible (top Kappa score of 0.631), accurately classifying the severity of motion remains an open challenge. In the RCS task, state-of-the-art methods achieved high accuracy on images with minimal motion. However, our analysis revealed a crucial finding: segmentation performance, and consequently the accuracy of derived clinical biomarkers, degrades significantly as motion artifacts increase. A notable performance gap also persists between the best algorithms and human experts, particularly in cases of severe motion. These results underscore the critical need for continued research into motion-robust analysis techniques, for which the *CMRxMotion* dataset will serve as a valuable, ongoing resource.

Declaration of interests

The authors declare that they have no known competing financial interests or personal relationships that could have appeared to influence the work reported in this paper.

Acknowledgments

Shuo Wang was supported in part by the National Key Research and Development Program of China (No. 2024YFF1207500), Shanghai Municipal Education Commission Project for Promoting Research Paradigm Reform and Empowering Disciplinary Advancement through Artificial Intelligence (SOF101020), and the International Science and Technology Cooperation Program

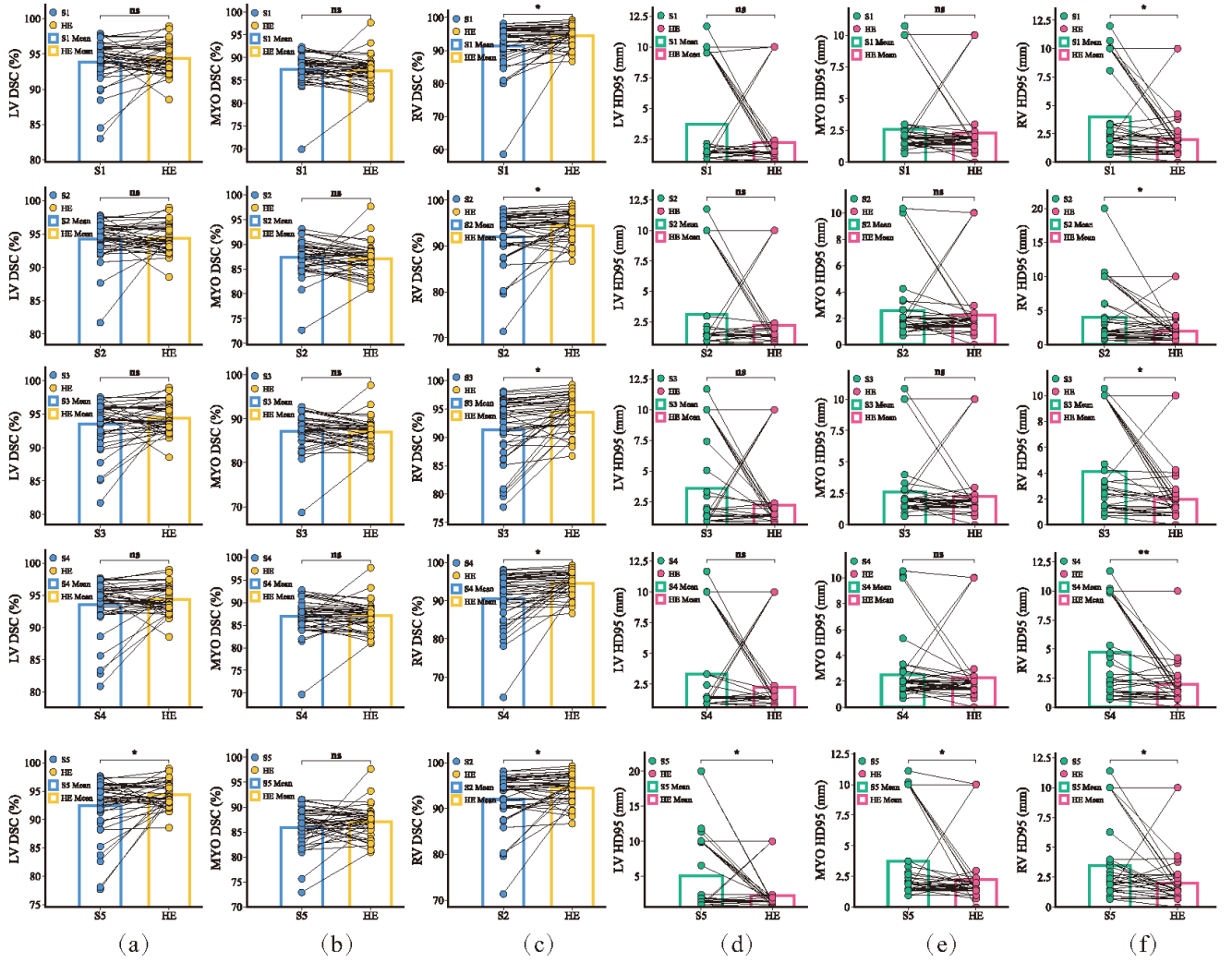


Figure 14: Paired t-test comparison between the top 3 AI models (S1-S5) and a human expert (HE) on 40 CMR volumes. The plots show performance for (a-c) DSC and (d-f) HD95 for the LV, MYO, and RV. **ns** indicates no significant difference, * indicates $p \leq 0.05$, and ** indicates $p \leq 0.001$.

Table 17: Evaluation of interobserver agreement of segmentation masks. The reported data are in the format of mean \pm standard deviation. \uparrow represents higher is better, \downarrow represents lower is better.

IQA Score	DSC (%) \uparrow			HD95 (mm) \downarrow		
	LV	MYO	RV	LV	MYO	RV
1	95.37 ± 2.02	88.06 ± 3.63	95.54 ± 2.64	1.72 ± 2.06	1.50 ± 0.56	1.59 ± 2.12
2	93.55 ± 2.16	86.05 ± 2.42	93.75 ± 3.26	2.98 ± 3.27	3.18 ± 3.19	2.26 ± 2.19
3	93.73 ± 0.95	86.76 ± 2.21	93.00 ± 2.33	1.55 ± 0.23	1.92 ± 0.06	2.41 ± 1.08

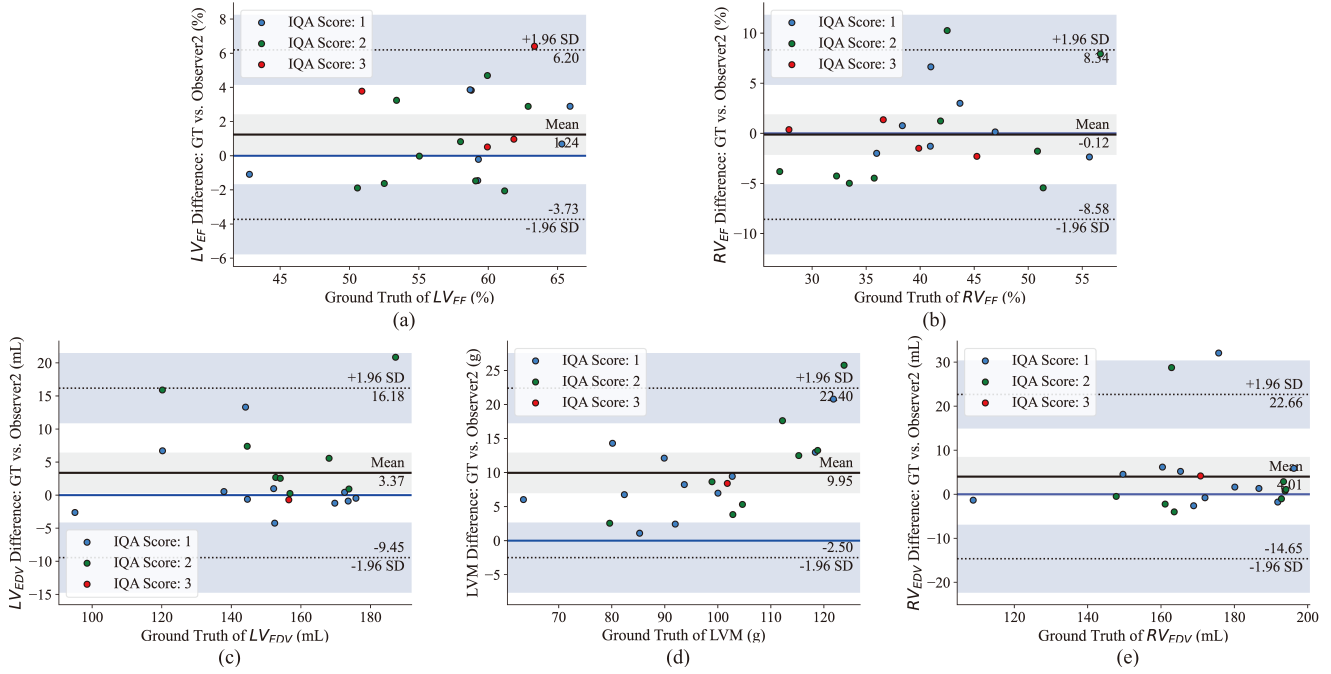


Figure 15: Bland-Altman plots illustrating the inter-observer agreement for the five clinical biomarkers. The solid black line indicates the mean difference, and the dashed lines represent the 95% limits of agreement.

under the 2023 Shanghai Action Plan for Science (23410710400). Chengyan Wang is supported by the Shanghai Municipal Science and Technology Major Project (No.2023SHZDZX02A05), the Shanghai Rising-Star Program (No.24QA2703300), and the National Key R&D Program of China (2024YFC3405800). Kang Wang is supported by Opening Laboratory Program of Linyi People's Hospital (No.2024LYKC001). Shi Zhang is supported by the National Natural Science Foundation of China (No. 82202145) and the Shanghai Magnolia Talent Program Pujiang Project (No. 2023PJD012).

We would like to thank all volunteers who generously took the time to participate in this study. We also extend our gratitude to Synapse and Paratera Technology Ltd for their technical support. The computations were performed using the CFFF platform of Fudan University.

CRediT authorship contribution statement

Kang Wang: Methodology, Software, Validation, Formal analysis, Investigation, Data Curation, Writing - Original Draft, Writing - Editing, Visualization, Funding acquisition; **Chen Qin:** Project administration, Conceptualization, Resources, Writing - Review & Editing, Supervision; **Zhang Shi:** Validation, Resources, Data curation, Funding acquisition; **Haoran Wang:** Software, Validation, Formal analysis, Data Curation; **Xiwen Zhang:** Formal analysis, Writing - Review & Editing, Data Curation; **Chen Chen:** Formal analysis, Validation, Resources, Writing - Review & Editing; **Cheng Ouyang:** Formal analysis, Validation, Resources, Writing - Review & Editing; **Chengliang Dai:** Validation, Resources, Data curation; **Yuanhan Mo:** Validation, Resources, Data curation; **Chenchen Dai:** Validation, Resources, Data curation; **Xutong Kuang:** Validation, Resources, Data curation; **Ruizhe Li:** Writing - Re-

view & Editing, Methodology, Software, Formal analysis; **Xin Chen:** Writing - Review & Editing, Methodology, Software, Formal analysis; **Xiuzheng Yue:** Writing - Review & Editing, Methodology, Software, Formal analysis; **Song Tian:** Writing - Review & Editing, Methodology, Software, Formal analysis; **Alejandro Mora-Rubio:** Writing - Review & Editing, Methodology, Software, Formal analysis; **Kumaradevan Punithakumar:** Writing - Review & Editing, Methodology, Software, Formal analysis; **Shizhan Gong:** Writing - Review & Editing, Methodology, Software, Formal analysis; **Qi Dou:** Writing - Review & Editing, Methodology, Software, Formal analysis; **Sina Amirrajab:** Writing - Review & Editing, Methodology, Software, Formal analysis; **Yasmina Al Khalil:** Writing - Review & Editing, Methodology, Software, Formal analysis; **Cian M. Scannell:** Writing - Review & Editing, Methodology, Software, Formal analysis; **Lexiaozhi Fan:** Writing - Review & Editing, Methodology, Software, Formal analysis; **Huili Yang:** Writing - Review & Editing, Methodology, Software, Formal analysis; **Xiaowu Sun:** Writing - Review & Editing, Methodology, Software, Formal analysis; **Rob van der Geest:** Writing - Review & Editing, Methodology, Software, Formal analysis; **Tewodros Weldebirhan Arega:** Writing - Review & Editing, Methodology, Software, Formal analysis; **Fabrice Meriaudeau:** Writing - Review & Editing, Methodology, Software, Formal analysis; **Caner Özer:** Writing - Review & Editing, Methodology, Software, Formal analysis; **Amin Ranem:** Writing - Review & Editing, Methodology, Software, Formal analysis; **John Kalkhof:** Writing - Review & Editing, Methodology, Software, Formal analysis; **İlkay Öksüz:** Writing - Review & Editing, Methodology, Software, Formal analysis; **Anirban Mukhopadhyay:** Writing - Review & Editing, Methodology, Software, Formal analysis; **Abdul Qayyum:** Writing - Review & Editing, Methodology, Software, For-

mal analysis; **Moona Mazher**: Writing - Review & Editing, Methodology, Software, Formal analysis; **Steven A Niederer**: Writing - Review & Editing, Methodology, Software, Formal analysis; **Carles Garcia-Cabrera**: Writing - Review & Editing, Methodology, Software, Formal analysis; **Eric Arazo**: Writing - Review & Editing, Methodology, Software, Formal analysis; **Michal K. Grzeszczyk**: Writing - Review & Editing, Methodology, Software, Formal analysis; **Szymon Płotka**: Writing - Review & Editing, Methodology, Software, Formal analysis; **Wanqin Ma**: Writing - Review & Editing, Methodology, Software, Formal analysis; **Xiaomeng Li**: Writing - Review & Editing, Methodology, Software, Formal analysis; **Rongjun Ge**: Writing - Review & Editing, Methodology, Software, Formal analysis; **Yongqing Kou**: Writing - Review & Editing, Methodology, Software, Formal analysis; **Xinrong Chen**: Validation, Resources, Data curation; **He Wang**: Formal analysis, Resources, Writing - Review & Editing; **Chengyan Wang**: Conceptualization, Resources, Writing - Review & Editing, Funding acquisition; **Wenjia Bai**: Conceptualization, Supervision, Formal analysis, Resources, Writing - Review & Editing, Software; **Shuo Wang**: Project administration, Conceptualization, Methodology, Validation, Formal analysis, Data curation, Writing - Original Draft, Writing - Review & Editing, Supervision, Funding acquisition.

Data availability

Access to the challenge data will be granted upon approval.

References

A., N., AJ., B., Andrew, A., Jonathan, M., Josette, B., kungvu, Meghan, O'Connell, Mike, K., RomanSalasnyk, Shannon, Steve, M., Will, C., 2015. Second annual data science bowl. URL: <https://kaggle.com/competitions/second-annual-data-science-bowl>.

Abraham, N., Khan, N.M., 2019. A novel focal tversky loss function with improved attention u-net for lesion segmentation, in: 2019 IEEE 16th International Symposium on Biomedical Imaging (ISBI 2019), pp. 683–687.

Ali, M., 2020. PyCaret: An open source, low-code machine learning library in Python. URL: <https://www.pycaret.org>. pyCaret version 3.0.

Amirrajab, S., Al Khalil, Y., Pluim, J., Breeuwer, M., Scannell, C.M., 2022. Cardiac MR Image Segmentation and Quality Control in the Presence of Respiratory Motion Artifacts Using Simulated Data, in: Statistical Atlases and Computational Models of the Heart. Regular and CMRx-Motion Challenge Papers, Springer Nature Switzerland, Cham. pp. 466–475.

Arega, T.W., Bricq, S., Meriaudeau, F., 2022. Automatic Quality Assessment of Cardiac MR Images with Motion Artefacts Using Multi-task Learning and K-Space Motion Artefact Augmentation, in: Statistical Atlases and Computational Models of the Heart. Regular and CMRx-Motion Challenge Papers, Springer Nature Switzerland, Cham. pp. 418–428.

Bai, W., Suzuki, H., Huang, J., Francis, C., Wang, S., Tarroni, G., Guitton, F., Aung, N., Fung, K., Petersen, S.E., Piechnik, S.K., Neubauer, S., Evangelou, E., Dehghan, A., O'Regan, D.P., Wilkins, M.R., Guo, Y., Matthews, P.M., Rueckert, D., 2020. A population-based phenome-wide association study of cardiac and aortic structure and function. *Nat. Med.* 26, 1654–1662. doi:10.1038/s41591-020-1009-y.

Baid, U., Ghodasara, S., Bilello, M., Mohan, S., Calabrese, E., Colak, E., Farahani, K., Kalpathy-Cramer, J., Kitamura, F.C., Pati, S., Prevedello, L.M., Rudie, J.D., Sako, C., Shinohara, R.T., Bergquist, T., Chai, R., Eddy, J.A., Elliott, J., Reade, W., Schaffter, T., Yu, T., Zheng, J., Annotators, B., Davatzikos, C., Mongan, J., Hess, C., Cha, S., Villanueva-Meyer, J.E., Freymann, J.B., Kirby, J.S., Wiestler, B., Crivellaro, P., Colen, R.R., Kotrotsou, A., Marcus, D.S., Milchenko, M., Nazeri, A., Fathallah-Shaykh, H.M., Wiest, R., Jakab, A., Weber, M., Mahajan, A., Menze, B.H., Flanders, A.E., Bakas, S., 2021. The RSNA-ASNR-MICCAI brats 2021 benchmark on brain tumor segmentation and radiogenomic classification. *arXiv preprint* , arXiv:2107.02314.

Benchoufi, M., Matzner-Lober, E., Molinari, N., Jannot, A.S., Soyer, P., 2020. Interobserver agreement issues in radiology. *Diagn. Interv. Imaging* 101, 639–641.

Bernard, O., Lalande, A., Zotti, C., Cervenansky, F., Yang, X., Heng, P.A., Cetin, I., Lekadir, K., Camara, O., Gonzalez Ballester, M.A., Sanroma, G., Napel, S., Petersen, S., Tziritas, G., Grinias, E., Khened, M., Kollerathu, V.A., Krishnamurthi, G., Rohé, M.M., Pennec, X., Sermesant, M., Isensee, F., Jäger, P., Maier-Hein, K.H., Full, P.M., Wolf, I., Engelhardt, S., Baumgartner, C.F., Koch, L.M., Wolterink, J.M., Işgum, I., Jang, Y., Hong, Y., Patravali, J., Jain, S., Humbert, O., Jodoin, P.M., 2018. Deep learning techniques for automatic mri cardiac multi-structures segmentation and diagnosis: Is the problem solved? *IEEE Trans. Med. Imaging* 37, 2514–2525.

Bristow, M.R., Kao, D.P., Breathett, K.K., Altman, N.L., Gorcsan, J., Gill, E.A., Lowes, B.D., Gilbert, E.M., Quaife, R.A., Mann, D.L., 2017. Structural and functional phenotyping of the failing heart. *JACC Heart Fail.* 5, 772–781.

Camara, O., Puyol-Antón, E., Qin, C., Sermesant, M., Suinesiaputra, A., Wang, S., Young, A., 2023. Statistical Atlases and Computational Models of the Heart. Regular and CMRxMotion Challenge Papers: 13th International Workshop, STACOM 2022, Held in Conjunction with MICCAI 2022, Singapore, September 18, 2022, Revised Selected Papers. volume 13593 of *Lecture Notes in Computer Science*. 1 ed., Springer, Cham.

Campello, V.M., Gkontra, P., Izquierdo, C., Martín-Isla, C., Sojoudi, A., Full, P.M., Maier-Hein, K., Zhang, Y.,

He, Z., Ma, J., Parreño, M., Albiol, A., Kong, F., Shadden, S.C., Acero, J.C., Sundaresan, V., Saber, M., Elattar, M., Li, H., Menze, B., Khader, F., Haarburger, C., Scannell, C.M., Veta, M., Carscadden, A., Punithakumar, K., Liu, X., Tsaftaris, S.A., Huang, X., Yang, X., Li, L., Zhuang, X., Viladés, D., Descalzo, M.L., Guala, A., Mura, L.L., Friedrich, M.G., Garg, R., Lebel, J., Henriques, F., Karakas, M., Çavuş, E., Petersen, S.E., Escalera, S., Seguí, S., Rodríguez-Palomares, J.F., Lekadir, K., 2021. Multi-centre, multi-vendor and multi-disease cardiac segmentation: The m&ms challenge. *IEEE Trans. Med. Imaging* 40, 3543–3554.

Cao, H., Wang, Y., Chen, J., Jiang, D., Zhang, X., Tian, Q., Wang, M., 2023. Swin-Unet: Unet-Like Pure Transformer for Medical Image Segmentation, in: Computer Vision – ECCV 2022 Workshops, Springer Nature Switzerland, Cham. pp. 205–218.

Cao, W., Mirjalili, V., Raschka, S., 2020. Rank consistent ordinal regression for neural networks with application to age estimation. *Pattern Recogn Lett* 140, 325–331.

Chen, C., Qin, C., Ouyang, C., Li, Z., Wang, S., Qiu, H., Chen, L., Tarroni, G., Bai, W., Rueckert, D., 2022. Enhancing MR image segmentation with realistic adversarial data augmentation. *Med. Image Anal.* 82, 102597.

Chen, C., Qin, C., Qiu, H., Tarroni, G., Duan, J., Bai, W., Rueckert, D., 2020. Deep learning for cardiac image segmentation: a review. *Front. Cardiovasc. Med.* 7, 25.

Chen, L.C., Papandreou, G., Schroff, F., Adam, H., 2017. Rethinking Atrous Convolution for Semantic Image Segmentation. arXiv preprint , arXiv:1706.05587.

Chen, X., He, K., 2021. Exploring simple siamese representation learning, in: Proc. IEEE/CVF Conf. Comput. Vis. Pattern Recog. (CVPR), pp. 15750–15758.

Chen, X., Yuan, Y., Zeng, G., Wang, J., 2021. Semi-Supervised Semantic Segmentation with Cross Pseudo Supervision. arXiv preprint , arXiv:2106.01226.

Deng, J., Dong, W., Socher, R., Li, L.J., Li, K., Fei-Fei, L., 2009. Imagenet: A large-scale hierarchical image database, in: Proc. IEEE/CVF Conf. Comput. Vis. Pattern Recog. (CVPR), pp. 248–255.

Dosovitskiy, A., Beyer, L., Kolesnikov, A., Weissenborn, D., Zhai, X., Unterthiner, T., Dehghani, M., Minderer, M., Heigold, G., Gelly, S., others, 2020. An image is worth 16x16 words: Transformers for image recognition at scale. arXiv preprint .

Dozat, T., 2015. Technical report, incorporating nesterov momentum into adam, in: Proc. ICLR Workshop, Ithaca, San Diego, CA, USA. pp. 7–9.

Eche, T., Schwartz, L.H., Mokrane, F.Z., Dercle, L., 2021. Toward generalizability in the deployment of artificial intelligence in radiology: Role of computation stress testing to overcome underspecification. *Radiol Artif Intell* 3, e210097.

Ferreira, P.F., Gatehouse, P.D., Mohiaddin, R.H., Firmin, D.N., 2013. Cardiovascular magnetic resonance artefacts. *J. Cardiovasc. Magn. Reson.* 15, 1–39.

Garcia-Cabrera, C., Arazo, E., Curran, K.M., O'Connor, N.E., McGuinness, K., 2022. Cardiac Segmentation Using Transfer Learning Under Respiratory Motion Artifacts, in: Statistical Atlases and Computational Models of the Heart. Regular and CMRxMotion Challenge Papers, Springer Nature Switzerland, Cham. pp. 392–398.

Gong, S., Lu, W., Xie, J., Zhang, X., Zhang, S., Dou, Q., 2022. Robust Cardiac MRI Segmentation with Data-Centric Models to Improve Performance via Intensive Pre-training and Augmentation, in: Statistical Atlases and Computational Models of the Heart. Regular and CMRx-Motion Challenge Papers, Springer Nature Switzerland, Cham. pp. 494–504.

González, C., Ranem, A., Pinto dos Santos, D., Othman, A., Mukhopadhyay, A., 2023. Lifelong nnU-Net: a framework for standardized medical continual learning. *Sci. Rep.* 13, 9381.

Grzeszczyk, M.K., Płotka, S., Sitek, A., 2022. Multi-task Swin Transformer for Motion Artifacts Classification and Cardiac Magnetic Resonance Image Segmentation, in: Statistical Atlases and Computational Models of the Heart. Regular and CMRxMotion Challenge Papers, Springer Nature Switzerland, Cham. pp. 409–417.

Hatamizadeh, A., Nath, V., Tang, Y., Yang, D., Roth, H.R., Xu, D., 2022. Swin UNETR: Swin Transformers for Semantic Segmentation of Brain Tumors in MRI Images, in: Brainlesion: Glioma, Multiple Sclerosis, Stroke and Traumatic Brain Injuries, Springer International Publishing, Cham. pp. 272–284.

He, K., Zhang, X., Ren, S., Sun, J., 2016. Deep residual learning for image recognition, in: Proc. IEEE/CVF Conf. Comput. Vis. Pattern Recog. (CVPR), pp. 770–778.

He, Y., Yang, G., Yang, J., Chen, Y., Kong, Y., Wu, J., Tang, L., Zhu, X., Dillenseger, J.L., Shao, P., Zhang, S., Shu, H., Coatrieux, J.L., Li, S., 2020. Dense biased networks with deep priori anatomy and hard region adaptation: Semi-supervised learning for fine renal artery segmentation. *Med. Image Anal.* 63, 101722.

Huang, G., Liu, Z., van der Maaten, L., Weinberger, K.Q., 2017. Densely connected convolutional networks, in: Proc. IEEE/CVF Conf. Comput. Vis. Pattern Recog. (CVPR), pp. 4700–4708.

Isensee, F., Jaeger, P.F., Kohl, S.A.A., Petersen, J., Maier-Hein, K.H., 2021. nnU-Net: a self-configuring method for deep learning-based biomedical image segmentation. *Nat. Methods* 18, 203–211.

Isensee, F., Jaeger, P.F., Kohl, S.A.A., Petersen, J., Maier-Hein, K.H., 2022. nnU-Net: a self-configuring method for deep learning-based biomedical image segmentation. URL: <https://github.com/MIC-DKFZ/nnUNet>.

Kou, Y., Ge, R., Zhang, D., 2022. 3D MRI Cardiac Segmentation Under Respiratory Motion Artifacts, in: Statistical Atlases and Computational Models of the Heart. Regular and CMRxMotion Challenge Papers, Springer Nature Switzerland, Cham. pp. 457–465.

Lee, C.Y., Xie, S., Gallagher, P., Zhang, Z., Tu, Z., 2015. Deeply-Supervised Nets, in: Proceedings of the Eighteenth International Conference on Artificial Intelligence and Statistics, PMLR, San Diego, California, USA. pp. 562–570.

Li, H., Jiang, S., Tian, S., Yue, X., Chen, W., Fan, Y., 2022. Automatic Image Quality Assessment and Cardiac Segmentation Based on CMR Images, in: Statistical Atlases and Computational Models of the Heart. Regular and CMRxMotion Challenge Papers, Springer Nature Switzerland, Cham. pp. 439–446.

Li, L., Wu, F., Wang, S., Luo, X., Martín-Isla, C., Zhai, S., Zhang, J., Liu, Y., Zhang, Z., Ankenbrand, M.J., Jiang, H., Zhang, X., Wang, L., Arega, T.W., Altunok, E., Zhao, Z., Li, F., Ma, J., Yang, X., Puybareau, E., Oksuz, I., Bricq, S., Li, W., Punithakumar, K., Tsafaris, S.A., Schreiber, L.M., Yang, M., Liu, G., Xia, Y., Wang, G., Escalera, S., Zhuang, X., 2023. MyoPS: A benchmark of myocardial pathology segmentation combining three-sequence cardiac magnetic resonance images. *Med. Image Anal.* 87, 102808.

Li, R., Chen, X., 2022. Motion-Related Artefact Classification Using Patch-Based Ensemble and Transfer Learning in Cardiac MRI, in: Statistical Atlases and Computational Models of the Heart. Regular and CMRxMotion Challenge Papers, Springer Nature Switzerland, Cham. pp. 429–438.

Ma, W., Yao, H., Lin, Y., Guo, J., Li, X., 2022. Semi-supervised Domain Generalization for Cardiac Magnetic Resonance Image Segmentation with High Quality Pseudo Labels, in: Statistical Atlases and Computational Models of the Heart. Regular and CMRxMotion Challenge Papers, Springer Nature Switzerland, Cham. pp. 383–391.

Maier, O., Menze, B.H., Gablentz, J.v.d., Häni, L., Heinrich, M.P., Liebrand, M., Winzeck, S., Basit, A., Bentley, P., Chen, L., Christiaens, D., Dutil, F., Egger, K., Feng, C., Glockner, B., Götz, M., Haeck, T., Halme, H.L., Havaei, M., Iftekharuddin, K.M., Jodoin, P.M., Kamnitsas, K., Kellner, E., Korvenoja, A., Larochelle, H., Ledig, C., Lee, J.H., Maes, F., Mahmood, Q., Maier-Hein, K.H., McKinley, R., Muschelli, J., Pal, C., Pei, L., Rangarajan, J.R., Reza, S.M.S., Robben, D., Rueckert, D., Salli, E., Suetens, P., Wang, C.W., Wilms, M., Kirschke, J.S., Krämer, U.M., Münte, T.F., Schramm, P., Wiest, R., Handels, H., Reyes, M., 2017. ISLES 2015 - A public evaluation benchmark for ischemic stroke lesion segmentation from multispectral MRI. *Med. Image Anal.* 35, 250–269.

Maier-Hein, L., Reinke, A., Kozubek, M., Martel, A.L., Arbel, T., Eisenmann, M., Hanbury, A., Jannin, P., Müller, H., Onogur, S., Saez-Rodriguez, J., van Ginneken, B., Kopp-Schneider, A., Landman, B.A., 2020. Bias: Transparent reporting of biomedical image analysis challenges. *Med. Image Anal.* 66, 101796. URL: <https://www.sciencedirect.com/science/article/pii/S1361841520301602>, doi:<https://doi.org/10.1016/j.media.2020.101796>.

Martín-Isla, C., Campello, V.M., Izquierdo, C., Kushibar, K., Sendra-Balcells, C., Gkontra, P., Sojoudi, A., Fulton, M.J., Arega, T.W., Punithakumar, K., Li, L., Sun, X., Al Khalil, Y., Liu, D., Jabbar, S., Queirós, S., Galati, F., Mazher, M., Gao, Z., Beetz, M., Tautz, L., Galazis, C., Varela, M., Hüllebrand, M., Grau, V., Zhuang, X., Puig, D., Zuluaga, M.A., Mohy-ud Din, H., Metaxas, D., Breeuwer, M., van der Geest, R.J., Noga, M., Bricq, S., Rentschler, M.E., Guala, A., Petersen, S.E., Escalera, S., Palomares, J.F.R., Lekadir, K., 2023. Deep learning segmentation of the right ventricle in cardiac mri: The m&ms challenge. *IEEE J. Biomed. Health Inform.* 27, 3302–3313.

Mast, T.P., James, C.A., Calkins, H., Teske, A.J., Tichnell, C., Murray, B., Loh, P., Russell, S.D., Velthuis, B.K., Judge, D.P., Dooijes, D., Tedford, R.J., van der Heijden, J.F., Tandri, H., Hauer, R.N., Abraham, T.P., Doevedans, P.A., te Riele, A.S.J.M., Cramer, M.J., 2017. Evaluation of Structural Progression in Arrhythmogenic Right Ventricular Dysplasia/Cardiomyopathy. *JAMA Cardiol.* 2, 293–302.

Milletari, F., Navab, N., Ahmadi, S.A., 2016. V-net: Fully convolutional neural networks for volumetric medical image segmentation, in: 2016 Fourth International Conference on 3D Vision (3DV), pp. 565–571.

Mora-Rubio, A., Noga, M., Punithakumar, K., 2022. Deep Learning Based Classification and Segmentation for Cardiac Magnetic Resonance Imaging with Respiratory Motion Artifacts, in: Statistical Atlases and Computational Models of the Heart. Regular and CMRxMotion Challenge Papers, Springer Nature Switzerland, Cham. pp. 399–408.

Myronenko, A., 2019. 3d mri brain tumor segmentation using autoencoder regularization, in: Brainlesion: Glioma, Multiple Sclerosis, Stroke and Traumatic Brain Injuries, Springer International Publishing, Cham. pp. 311–320.

Paschali, M., Conjeti, S., Navarro, F., Navab, N., 2018. Generalizability vs. robustness: investigating medical imaging networks using adversarial examples, in: Proc. Int. Conf. Med. Image Comput. Comput.-Assisted Intervention, Springer. pp. 493–501.

Petitjean, C., Zuluaga, M.A., Bai, W., Dacher, J.N., Grosorge, D., Caudron, J., Ruan, S., Ayed, I.B., Cardoso, M.J., Chen, H.C., Jimenez-Carretero, D., Ledesma-Carbayo, M.J., Davatzikos, C., Doshi, J., Erus, G., Maier, O.M.O., Nambakhsh, C.M.S., Ou, Y., Ourselin, S., Peng, C.W., Peters, N.S., Peters, T.M., Rajchl, M., Rueckert, D., Santos, A., Shi, W., Wang, C.W., Wang, H., Yuan, J., 2015. Right ventricle segmentation from cardiac MRI: A collaboration study. *Med. Image Anal.* 19, 187–202.

Pérez-García, F., Sparks, R., Ourselin, S., 2021. TorchIO: A Python library for efficient loading, preprocessing, augmentation and patch-based sampling of medical images in deep learning. *Comput. Methods Programs Biomed.* 208, 106236.

Qayyum, A., Mazher, M., Niederer, S., Meriaudeau, F., Razzak, I., 2022. Automatic Cardiac Magnetic Resonance Respiratory Motions Assessment and Segmentation, in: Statistical Atlases and Computational Models of the Heart. Regular and CMRxMotion Challenge Papers, Springer Nature Switzerland, Cham. pp. 485–493.

Radau, P., Lu, Y., Connelly, K., Paul, G., Dick, A.J., Wright, G.A., 2009. Evaluation framework for algorithms segmenting short axis cardiac mri. *The MIDAS Journal* .

Ranem, A., González, C., Mukhopadhyay, A., 2022a. Continual hippocampus segmentation with transformers, in: Proc. IEEE/CVF Conf. Comput. Vis. Pattern Recog. (CVPR) Workshops, pp. 3711–3720.

Ranem, A., Kalkhof, J., Özer, C., Mukhopadhyay, A., Ok-suz, I., 2022b. Detecting Respiratory Motion Artefacts for Cardiovascular MRIs to Ensure High-Quality Segmentation, in: Statistical Atlases and Computational Models of the Heart. Regular and CMRxMotion Challenge Papers, Springer Nature Switzerland, Cham. pp. 447–456.

Ronneberger, O., Fischer, P., Brox, T., 2015. U-Net: Convolutional Networks for Biomedical Image Segmentation, in: Proc. Int. Conf. Med. Image Comput. Comput.-Assisted Intervention, Springer. pp. 234–241.

Schulz-Menger, J., Bluemke, D.A., Bremerich, J., Flamm, S.D., Fogel, M.A., Friedrich, M.G., Kim, R.J., von Knobelsdorff-Brenkenhoff, F., Kramer, C.M., Pennell, D.J., Plein, S., Nagel, E., 2020. Standardized image interpretation and post-processing in cardiovascular magnetic resonance - 2020 update. *J. Cardiovasc. Magn. Reson.* 22, 19. doi:10.1186/s12968-020-00610-6.

Shaw, R., Sudre, C., Ourselin, S., Cardoso, M.J., 2019. Mri k-space motion artefact augmentation: Model robustness and task-specific uncertainty, in: Proc. Int. Conf. Medical Imaging Deep Learn. (MIDL), PMLR. pp. 427–436.

Shi, X., Cao, W., Raschka, S., 2023. Deep neural networks for rank-consistent ordinal regression based on conditional probabilities. *Pattern Anal. Appl.* 26, 941–955.

Suinesiaputra, A., Cowan, B.R., Al-Agamy, A.O., Elattar, M.A., Ayache, N., Fahmy, A.S., Khalifa, A.M., Medrano-Gracia, P., Jolly, M.P., Kadish, A.H., Lee, D.C., Margeta, J., Warfield, S.K., Young, A.A., 2014. A collaborative resource to build consensus for automated left ventricular segmentation of cardiac MR images. *Med. Image Anal.* 18, 50–62.

Sun, X., Cheng, L.H., van der Geest, R.J., 2022. Combination Special Data Augmentation and Sampling Inspection Network for Cardiac Magnetic Resonance Imaging Quality Classification, in: Statistical Atlases and Computational Models of the Heart. Regular and CMRxMotion Challenge Papers, Springer Nature Switzerland, Cham. pp. 476–484.

Tan, M., Le, Q.V., 2019. EfficientNet: Rethinking Model Scaling for Convolutional Neural Networks. arXiv preprint , 1905.11946.

Tang, Y., Yang, D., Li, W., Roth, H.R., Landman, B., Xu, D., Nath, V., Hatamizadeh, A., 2022. Self-supervised pre-training of swin transformers for 3d medical image analysis, in: Proc. IEEE/CVF Conf. Comput. Vis. Pattern Recog. (CVPR), pp. 20730–20740.

Tobon-Gomez, C., Geers, A.J., Peters, J., Weese, J., Pinto, K., Karim, R., Ammar, M., Daoudi, A., Margeta, J., Sandoval, Z., Stender, B., Zheng, Y., Zuluaga, M.A., Betancur, J., Ayache, N., Chikh, M.A., Dillenseger, J.L., Kelm, B.M., Mahmoudi, S., Ourselin, S., Schlaefer, A., Schaeffter, T., Razavi, R., Rhode, K.S., 2015. Benchmark for algorithms segmenting the left atrium from 3d ct and mri datasets. *IEEE Trans. Med. Imaging* 34, 1460–1473.

Van Leemput, K., Maes, F., Vandermeulen, D., Suetens, P., 1999. Automated model-based tissue classification of mr images of the brain. *IEEE Trans. Med. Imaging* 18, 897–908.

Wang, C., Li, Y., Lv, J., Jin, J., Hu, X., Kuang, X., Chen, W., Wang, H., 2021a. Recommendation for cardiac magnetic resonance imaging-based phenotypic study: imaging part. *Phenomics* 1, 151–170.

Wang, S., Qin, C., Savioli, N., Chen, C., O'Regan, D.P., Cook, S., Guo, Y., Rueckert, D., Bai, W., 2021b. Joint motion correction and super resolution for cardiac segmentation via latent optimisation, in: Proc. Int. Conf. Med. Image Comput. Comput.-Assisted Intervention, Springer. pp. 14–24.

Wang, S., Qin, C., Wang, C., Wang, K., Wang, H., Chen, C., Ouyang, C., Kuang, X., Dai, C., Mo, Y., Shi, Z., Dai, C., Chen, X., Wang, H., Bai, W., 2022. The Extreme Cardiac MRI Analysis Challenge under Respiratory Motion (CM-RxMotion). arXiv e-prints , arXiv:2210.06385doi:10.48550/arXiv.2210.06385, arXiv:2210.06385.

Wang, S., Tarroni, G., Qin, C., Mo, Y., Dai, C., Chen, C., Glocker, B., Guo, Y., Rueckert, D., Bai, W., 2020. Deep generative model-based quality control for cardiac mri segmentation, in: Proc. Int. Conf. Med. Image Comput. Comput.-Assisted Intervention, Springer. pp. 88–97.

Xiong, Z., Xia, Q., Hu, Z., Huang, N., Bian, C., Zheng, Y., Vesal, S., Ravikumar, N., Maier, A., Yang, X., Heng, P.A., Ni, D., Li, C., Tong, Q., Si, W., Puybareau, E., Khoudli, Y., Géraud, T., Chen, C., Bai, W., Rueckert, D., Xu, L., Zhuang, X., Luo, X., Jia, S., Sermesant, M., Liu, Y., Wang, K., Borra, D., Masci, A., Corsi, C., de Vente, C., Veta, M., Karim, R., Preetha, C.J., Engelhardt, S., Qiao, M., Wang, Y., Tao, Q., Nuñez-Garcia, M., Camara, O., Savioli, N., Lamata, P., Zhao, J., 2021. A global benchmark of algorithms for segmenting the left atrium from late gadolinium-enhanced cardiac magnetic resonance imaging. *Med. Image Anal.* 67, 101832.

Yang, H., Fan, L., Iakovlev, N., Kim, D., 2022. A Deep Learning-Based Fully Automatic Framework for Motion-Existing Cine Image Quality Control and Quantitative Analysis, in: Statistical Atlases and Computational Models of the Heart. Regular and CMRxMotion Challenge Papers, Springer Nature Switzerland, Cham. pp. 505–512.

Yao, H., Hu, X., Li, X., 2022. Enhancing Pseudo Label Quality for Semi-Supervised Domain-Generalized Medical Image Segmentation. arXiv preprint , arXiv:2201.08657.

Zhang, D., Icke, I., Dogdas, B., Parimal, S., Sampath, S., Forbes, J., Bagchi, A., Chin, C.L., Chen, A., 2018. A multi-level convolutional lstm model for the segmentation of left ventricle myocardium in infarcted porcine cine mr images, in: 2018 IEEE 15th International Symposium on Biomedical Imaging (ISBI 2018), pp. 470–473.

Zhuang, X., 2016. Multivariate Mixture Model for Cardiac Segmentation from Multi-Sequence MRI, in: Proc. Int. Conf. Med. Image Comput. Comput.-Assisted Intervention, Springer. pp. 581–588.

Zhuang, X., 2019. Multivariate mixture model for myocardial segmentation combining multi-source images. IEEE Trans. Pattern Anal. Mach. Intell. 41, 2933–2946.

Zhuang, X., Li, L., Payer, C., Štern, D., Urschler, M., Heinrich, M.P., Oster, J., Wang, C., Smedby, O., Bian, C., Yang, X., Heng, P.A., Mortazi, A., Bagci, U., Yang, G., Sun, C., Galisot, G., Ramel, J.Y., Brouard, T., Tong, Q., Si, W., Liao, X., Zeng, G., Shi, Z., Zheng, G., Wang, C., MacGillivray, T., Newby, D., Rhode, K., Ourselin, S., Mohiaddin, R., Keegan, J., Firmin, D., Yang, G., 2019. Evaluation of algorithms for multi-modality whole heart segmentation: An open-access grand challenge. Med. Image Anal. 58, 101537.